



THE UNIVERSITY *of* EDINBURGH

Edinburgh Research Explorer

## Transition boundaries and an order-to-chaos map for the flow field past a flapping foil

**Citation for published version:**

Majumdar, D, Bose, C & Sarkar, S 2022, 'Transition boundaries and an order-to-chaos map for the flow field past a flapping foil', *Journal of Fluid Mechanics*, vol. 942, A40. <https://doi.org/10.1017/jfm.2022.385>

**Digital Object Identifier (DOI):**

[10.1017/jfm.2022.385](https://doi.org/10.1017/jfm.2022.385)

**Link:**

[Link to publication record in Edinburgh Research Explorer](#)

**Document Version:**

Publisher's PDF, also known as Version of record

**Published In:**

Journal of Fluid Mechanics

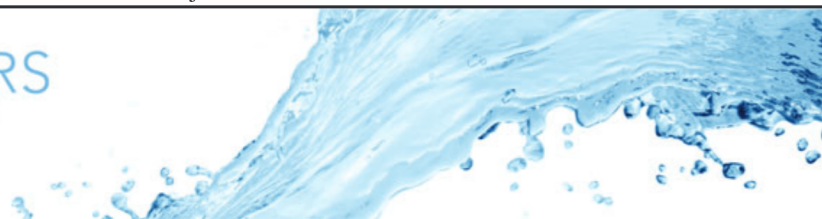
**General rights**

Copyright for the publications made accessible via the Edinburgh Research Explorer is retained by the author(s) and / or other copyright owners and it is a condition of accessing these publications that users recognise and abide by the legal requirements associated with these rights.

**Take down policy**

The University of Edinburgh has made every reasonable effort to ensure that Edinburgh Research Explorer content complies with UK legislation. If you believe that the public display of this file breaches copyright please contact [openaccess@ed.ac.uk](mailto:openaccess@ed.ac.uk) providing details, and we will remove access to the work immediately and investigate your claim.





# Transition boundaries and an order-to-chaos map for the flow field past a flapping foil

Dipanjana Majumdar<sup>1</sup>, Chandan Bose<sup>2</sup> and Sunetra Sarkar<sup>1,†</sup>

<sup>1</sup>Department of Aerospace Engineering, Indian Institute of Technology Madras, Chennai 600036, India

<sup>2</sup>Department of Aerospace and Mechanical Engineering, University of Liège, Liège 4000, Belgium

(Received 8 April 2021; revised 10 April 2022; accepted 26 April 2022)

The present study focuses on identifying dynamical transition boundaries and presents an order-to-chaos map for the unsteady flow field of a flapping foil in the low Reynolds number regime. The effect of an extensive parametric space, covering a large number of kinematic conditions, has been investigated. It is shown that the conventional non-dimensional parameters cannot effectively capture the changes in the flow field due to the variations in the relevant kinematic parameters and are unable to demarcate the dynamical transition boundaries. Two new non-dimensional measures – maximum effective angle of attack and a leading-edge amplitude-based Strouhal number – are proposed here, which can capture the physical effect of the parametric variations on the wake dynamics. The study proposes generalised transition boundaries and an order-to-chaos map through a transitional regime in terms of these two newly proposed parameters. Published data from the existing literature have also been tested to verify the proposed transition model. It is seen that despite the wide variety of the parametric combinations, the dynamical states from both the new and the published data corroborate well the proposed boundaries, giving credibility to the order-to-chaos map.

**Key words:** wakes

## 1. Introduction

A systematic resolution of the nonlinear dynamical transitions in the near and far wake of flapping bodies is still elusive. In the aperiodic and chaotic regimes, the aerodynamic loads acting on a flapping body can become unpredictable from one flapping cycle to another, posing significant challenges in designing suitable control algorithms for

† Email address for correspondence: [sunetra.sarkar@gmail.com](mailto:sunetra.sarkar@gmail.com)

© The Author(s), 2022. Published by Cambridge University Press. This is an Open Access article, distributed under the terms of the Creative Commons Attribution licence (<https://creativecommons.org/licenses/by/4.0/>), which permits unrestricted re-use, distribution, and reproduction in any medium, provided the original work is properly cited.

man-made flapping devices. Therefore, kinematic parameters that lead to aperiodic/chaotic flow dynamics are not desirable from the viewpoint of an efficient design of bio-inspired flapping devices like micro aerial vehicles. Identifying the transition onsets to determine a stable operating regime for such devices is important. Earlier studies in the literature are focused primarily on von Kármán to reverse von Kármán wake (drag-to-thrust) transition (Triantafyllou, Triantafyllou & Gopalkrishnan 1991; Streitlien & Triantafyllou 1998) and symmetric to deflected wake transition phenomena (Jones, Dohring & Platzer 1998; Godoy-Diana *et al.* 2009; Zheng & Wei 2012); note that both transitions happen in the periodic regime. However, a few recent studies have also highlighted interesting changes from periodicity to aperiodicity in the wake for different canonical flapping kinematics, e.g. pure plunging (Lewin & Haj-Hariri 2003; Badrinath, Bose & Sarkar 2017; Majumdar, Bose & Sarkar 2020a), pure pitching (Zaman, Young & Lai 2017) and combined pitching–plunging (Lentink *et al.* 2010; Bose & Sarkar 2018; Bose, Gupta & Sarkar 2021). Different local bifurcation routes to chaos, involving quasi-periodic and intermittent dynamical states, were reported in these studies.

Lentink *et al.* (2010), through two-dimensional (2-D) soap film experiments, presented chaotic wake patterns using phase-averaged vorticity contours. Bose & Sarkar (2018) and Bose *et al.* (2021), through Navier–Stokes simulations, reported a quasi-periodic route, accompanied by sporadic intermittent windows of aperiodicity, towards a regime of robust chaos. The authors established that the time delay in the formation of the primary leading-edge vortex (LEV) was instrumental in ushering chaos in the wake. At high plunge velocities, the LEV sheds aperiodically, and subsequently, its irregular interactions with the trailing-edge vortex (TEV) gives way to chaos in the wake. The mechanism is sustained in the far wake through a variety of fundamental vortex interactions (such as vortex merging, collision, shredding, exchange of partners). Majumdar *et al.* (2020a) have also shown that the aperiodic transition is extremely sensitive to LEV behaviour, and any discrepancy in their formation, growth or transport may lead to a completely different dynamical state. Note that even though the effects of flapping amplitude and frequency were considered carefully in these earlier studies, some of the other important kinematic parameters, such as pitch amplitude, pitching axis location, phase offset and kinematic pattern, have received almost no attention in the existing literature. In the case of combined kinematics, it is likely that LEV separation, and in turn, the near-field interactions of vortices, will be altered significantly by varying these parameters. Furthermore, the ensuing change in the effective angle of attack (AoA) for combined pitch and plunge can also be crucial in dictating the flow field. Note that earlier studies that considered the variation of some of these parameters (Anderson *et al.* 1998; Read, Hover & Triantafyllou 2003; Lee & Su 2015; Buren, Floryan & Smits 2019) focused primarily on their effect on aerodynamic force magnitudes and pressure distributions, and not on dynamical behaviour. No attempts have yet been made in the existing literature to consider the effects of all these relevant parametric combinations together and study the dynamical transitions to predict generalised bifurcation boundaries.

This leads to two interesting directions: first, can one identify suitable non-dimensional parameters that can capture the effects of different kinematic parameters together, and second, can one model generalised transition/bifurcation boundaries to demarcate the dynamical regimes to an acceptable level of accuracy, statistically? Traditionally, flow field transitions have been defined in terms of a diverse set of non-dimensional parameters. Godoy-Diana *et al.* (2009) demonstrated the wake transition for a pure pitching kinematics using an ' $A_D$  versus  $St_D$ ' plot, where  $A_D$  is the thickness-based dimensionless

amplitude, and  $St_D$  is the thickness-based Strouhal number. Here,  $A_D = A/D$ , where  $A$  and  $D$  represent the peak-to-peak amplitude of the trailing edge and the maximum thickness of the foil, respectively;  $St_D = f_e D/U_\infty$ , where  $f_e$  and  $U_\infty$  denote the flapping frequency and free stream velocity, respectively. Deng *et al.* (2016) have used the same parameters and have presented periodic to chaotic transitions for increasing  $St_D$  at a fixed  $A_D$ . Cleaver, Wang & Gursul (2012) presented flow field bifurcations in terms of the chord-based Strouhal number  $St_c$ , where  $St_c = f_e c/U_\infty$ , with  $c$  being the chord length. Triantafyllou *et al.* (1991) defined an amplitude-based Strouhal number as  $St_A = f_e A/U_\infty$ , to characterise the drag-to-thrust transition. It was proposed as the single key parameter that is a function of both flapping amplitude and frequency simultaneously. Lewin & Haj-Hariri (2003), Lentink *et al.* (2010) and Ashraf, Young & Lai (2012), as well as the recent studies from our group (Bose & Sarkar 2018; Majumdar *et al.* 2020a), have considered the maximum non-dimensional plunge velocity ( $\kappa h$ ) as the main control parameter for wake transitions. Here,  $\kappa h$  is proportional to  $St_A$ , where  $\kappa = 2\pi f_e c/U_\infty$  is called the reduced frequency and  $h = h_0/c$  is the non-dimensional plunge amplitude.

Note that these existing non-dimensional parameters are not comprehensive enough to encompass the combined effects of different kinematic conditions. Previous studies that consider simple and unmixed kinematics, such as pure pitching or pure plunging, rely on a fixed set of dimensionless parameters that are effective enough to identify the changes in the flow field. However, they fall short in reflecting the combined effects of multiple parameters in a wholesome manner when more complex kinematics are used. These kinematic parameters include phase offsets between simple canonical kinematics and location of the pitching axis. Also, the parametric maps available in the literature for distinguishing qualitatively different wake regimes are strongly kinematic-specific and are mostly applicable to the periodic regime (low  $\kappa h$  or  $St_A$ ). To address this issue, Lagopoulos, Weymouth & Ganapathisubramani (2019) have defined a path-length-based Strouhal number  $St_\tau = f_e \tau/U_\infty$ , where  $\tau$  is the average trajectory length covered by the chord of the foil in one flapping period. It was reported that, irrespective of the flapping kinematics, drag-to-thrust transition takes place as  $St_\tau$  crosses unity. However, the applicability of  $St_\tau$  was confined to the periodic flow regime only ( $0.15 < St_D < 0.35$ ). No attempts have yet been made in the literature to demarcate the regimes of aperiodic transitions using a robust measure considering the combined effects of all the relevant kinematic parameters of importance. The present study is focused in that direction with the following specific objectives: (i) to establish the role of a wide variety of kinematic parameters, including plunge amplitude ( $h$ ), pitch amplitude ( $\theta_0$ ), reduced frequency ( $\kappa$ ), pitching axis location ( $x_0$ ), elliptic foil thickness, flapping kinematics, and phase offset ( $\phi$ ) on the dynamical transition of the wake from order to chaos; (ii) to identify new non-dimensional measures encompassing the effects of all important kinematic quantities, and present an order-to-chaos map, demarcating the periodic, quasi-periodic/intermittency and chaotic states; (iii) to propose mathematical models for the generalised transition boundaries for predicting the transition onsets. Overall, this study aims to provide novel metrics connected to wake transitions and insight into the underlying flow field mechanisms behind chaos.

The present study is limited to 2-D situations, and the authors are not in a position to comment on three-dimensional (3-D) behaviour through the present set of results. The 3-D wake interactions for a finite-span wing can be distinctly different as compared to the 2-D flow field in the presence of tip vortices (Calderon *et al.* 2014). Apart from the tip vortices, an LEV can also be instrumental in giving rise to spanwise instability. Very recently,

Zurman-Nasution, Ganapathisubramani & Weymouth (2020) studied comprehensively the effect of three-dimensionality on the propulsive performance of flapping wings, and reported that the balance between the strength and stability of leading/trailing-edge vortices and the flapping energy underlies the trigger for 2-D to 3-D transition. The authors also stated that 2-D simulation results remain comparable to those obtained from 3-D simulations within a certain range of the flapping amplitude/frequency. However, the parametric range at which significant qualitative differences between the 2-D and 3-D structures are expected is not entirely conclusive. Visbal (2009) reported that 2-D leading-edge coherent vortices can break down into small-scale 3-D structures, preventing chaotic wakes in three dimensions. Note that this behaviour has been reported at Reynolds number ranges higher by at least an order of magnitude than the present case. A subsequent study by Ashraf *et al.* (2012) took up this question more systematically and confirmed that such observations were confined to high-frequency low-amplitude regimes only. However, at relatively low-frequency and high-amplitude situations (as considered in the present study as well), the 2-D primary structures were found to be stable and were also qualitatively similar to the corresponding 3-D structures (with small variation in the secondary structures). Note that the scope of the present 2-D study has been kept limited to low-frequency and high-amplitude flapping motions.

The rest of the paper is organised as follows. A brief description of the flapping motion and the computational methodologies are provided in § 2. The transitional wake dynamics observed at variety of parametric combinations are presented in § 3. Section 4 explains the role of the primary LEV in dictating the dynamical characteristic of the flow field and the role of phase offset in altering LEV behaviour. Non-dimensional measures and a mathematical model of generalised transition boundaries to distinguish the different dynamical regimes are proposed in § 5. The salient findings are summarised and conclusions are drawn in § 6.

## 2. Computational details

### 2.1. Body geometry and flapping kinematics

A rigid elliptic foil is subjected to a simultaneous pitching–plunging motion under a uniform inflow condition. The location of the pitching axis along the chord is represented by  $x_0$ , which indicates the distance of the pivot location from the leading edge of the foil. Unless mentioned specifically otherwise, a sinusoidal flapping kinematics is used in the present study as follows:

$$y_p(t) = h_0 \sin(2\pi f_e t), \quad (2.1)$$

$$\theta(t) = \theta_m + \theta_0 \sin(2\pi f_e t + \phi), \quad (2.2)$$

where  $y_p$  denotes the position of the pivot point in the vertical direction, and  $\theta$  is the instantaneous pitching rotation, defined clockwise positive. Here,  $h_0$  is the plunge amplitude;  $\theta_0$  denotes the pitch amplitude, and  $\theta_m$  signifies the mean pitch angle and is chosen to be zero ( $\theta_m = 0^\circ$ ) throughout this study;  $t$  indicates time. The phase offset between the plunging and pitching motions is denoted by  $\phi$ . Schematic drawings displaying the flapping motion of the foil are presented in figure 1, considering  $x_0 = 0.5$ , i.e. the pitching axis being at the mid-chord location. The thickness to chord ratio of the elliptic-shaped foil will be denoted as  $t_h/c$  (=minor axis/major axis). Throughout this study, time-instant values are presented by normalising them using the flapping period  $T(= 1/f_e)$ .

## Transition boundaries and an order-to-chaos map

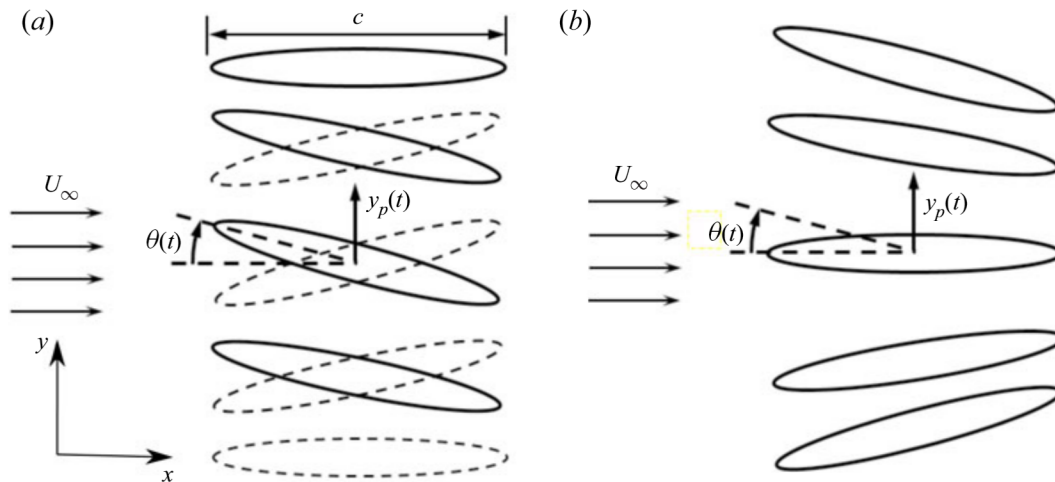


Figure 1. Position of the foil with pitch–plunge flapping kinematics for (a)  $\phi = \pi/2$ , where the leading edge leads the trailing edge and ‘slices through’ the incoming flow, and (b)  $\phi = 2\pi$ , where the foil appears to be pitching about a point downstream of the trailing edge. The solid lines indicate the upstroke, and the dashed lines indicate the downstroke.

### 2.2. The immersed boundary method based flow solver

The unsteady flow field is simulated by solving numerically the 2-D incompressible Navier–Stokes equation. A discrete forcing type immersed boundary method (IBM) based in-house flow solver (Majumdar *et al.* 2020a) is used in this study. In the present IBM technique, a ‘momentum forcing’ is applied at all the grid points inside the solid domain. This reconstructs the velocity field in the solid domain in such a way that the appropriate no-slip/no-penetration boundary condition is satisfied exactly on the solid surface (Kim, Kim & Choi 2001). Moreover, a mass source/sink term is included in the continuity equation to ensure rigorous mass conservation across the immersed boundary. A finite volume based semi-implicit fractional step method (FSM) of  $\Delta p$  form is adopted in the present work to advance discretised equations in time. In order to achieve a divergence-free velocity field, a pseudo pressure correction term is used to correct the intermediate velocities at every time step. The convection and diffusion terms are advanced in time using the Adams–Bashforth discretisation and the Crank–Nicolson method, respectively. The spatial derivatives are calculated using the second-order central difference scheme.

The flow Reynolds number is defined as  $Re = U_\infty c / \nu$ , with  $\nu$  being the kinematic viscosity of the fluid. A flow Reynolds number  $Re = 300$  is kept constant for all the simulations of present study. The drag ( $D'$ ) and lift ( $L'$ ) forces on the flapping foil are defined positive along the directions of the positive  $x$ - and  $y$ -axes, respectively. The aerodynamic load coefficients are computed as  $C_D = D' / 0.5 \rho_f U_\infty^2 c$  and  $C_L = L' / 0.5 \rho_f U_\infty^2 c$ , where  $\rho_f$  denotes the fluid density.

The flow-governing equations are solved on a background Eulerian grid, with the primitive flow variables ( $u, v, p$ ) being arranged in a staggered manner. At every time step, the position of the elliptic foil is tracked using 1500 Lagrangian markers. A rectangular computational domain consisting of a structured non-uniform Cartesian mesh is considered in this study. A uniform grid spacing of  $\Delta x \times \Delta y$  is used in the region of body movement, and then the grid spacing is increased following a geometric progression towards the outer boundaries. The mesh is stretched with common ratio 1.10 in the upstream direction, and common ratio 1.008 in the downstream side. In both top and

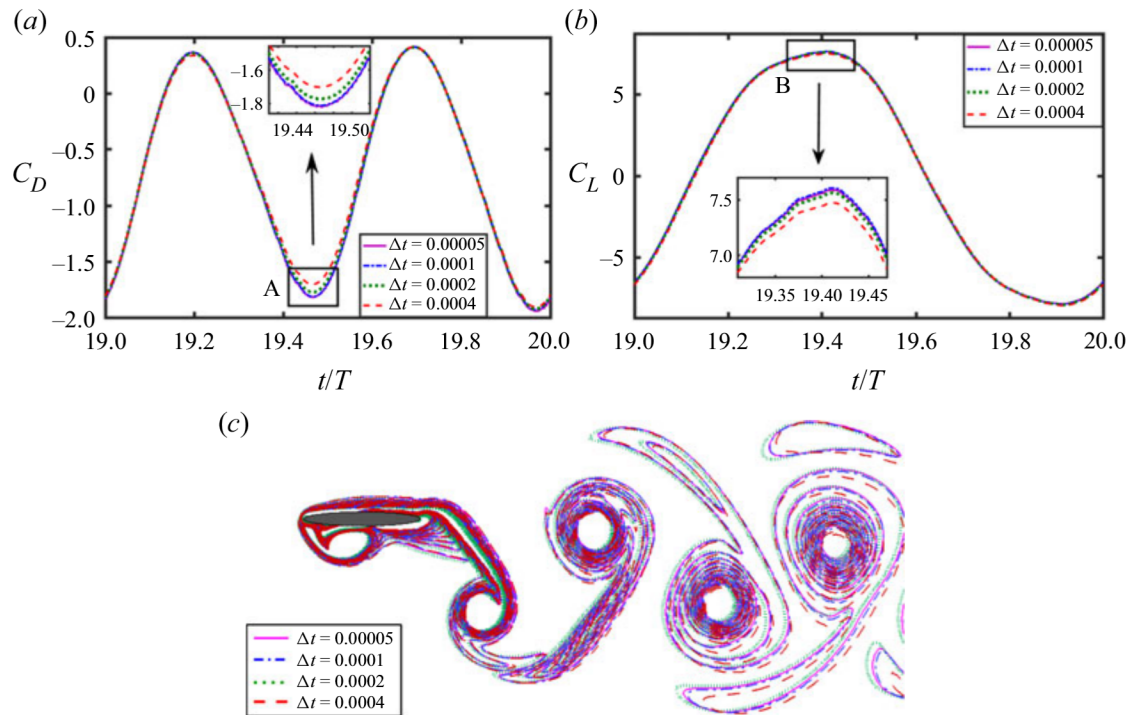


Figure 2. Time step independence test for the flow over a pitching–plunging foil: (a) drag and (b) lift coefficients, and (c) instantaneous vorticity contours at a typical time instant  $t/T = 20.25$ .

bottom directions, the mesh is stretched with common ratio 1.05. The boundary conditions are as follows: uniform inflow ( $u = 1, v = 0$ ), zero-gradient outflow ( $\partial u / \partial x = 0$ ), and the slip boundary condition ( $\partial u / \partial y = 0, v = 0$ ) at the top and bottom boundaries. Further details on the flow solver can be found in the earlier work by Majumdar *et al.* (2020a). It was also validated thoroughly in Majumdar *et al.* (2020a) by comparing the results of the present solver with those available in the literature, and also with the results obtained from a well-established ALE based OpenFOAM solver. The convergence test results relevant to the present study are presented next. Note that the time step size ( $\Delta t$ ), grid spacing ( $\Delta x$  and  $\Delta y$ ) and domain size reported in the next subsection are in their corresponding non-dimensional forms.

### 2.3. Convergence tests

For all the convergence test cases, simulations are performed for a simultaneously pitching–plunging elliptic foil with parametric set  $h = 0.375, \theta_0 = 15^\circ, \phi = \pi/2, \kappa = 4.0, x_0 = 0.5, t_h/c = 0.12$  and  $Re = 300$ , which corresponds to a periodic flow field.

#### 2.3.1. Time step convergence test

An appropriate time step size has been chosen through a time step independence test with four different time step sizes,  $\Delta t = 0.00005, 0.0001, 0.0002$  and  $0.0004$ . The grid size in the uniform mesh region is taken as  $\Delta x = \Delta y = 0.004$ , with the mesh stretching ratios towards the outer boundaries being the same as mentioned in § 2.2. The size of the computational domain is considered to be  $[-10.0, 30.0] \times [-12.5, 12.5]$  along the  $x$ - and  $y$ -axes, respectively. Time histories of  $C_D$  and  $C_L$  along with close-up views near the peaks, and instantaneous vorticity contours at a typical time instant ( $t/T = 20.25$ ), are presented in figure 2. Vorticity contour plots are shown considering vorticity range  $-10$  to

Time step size	Peak lift coefficient ( $C_L^{peak}$ )	Mean drag coefficient ( $\bar{C}_D$ )
$\Delta t = 0.0004$	7.5411 (0.83 %)	-0.7078 (4.75 %)
$\Delta t = 0.0002$	7.5601 (0.58 %)	-0.7255 (2.37 %)
$\Delta t = 0.0001$	7.5947 (0.13 %)	-0.7398 (0.44 %)
$\Delta t = 0.00005$	7.6046	-0.7431

Table 1. Results of time step convergence study; the values in parentheses denote percentage relative difference with respect to corresponding values of the lowest  $\Delta t$  case.

Mesh size	Peak lift coefficient ( $C_L^{peak}$ )	Mean drag coefficient ( $\bar{C}_D$ )
$\Delta x = \Delta y = 0.008$	7.4625 (1.9 %)	-0.7188 (2.98 %)
$\Delta x = \Delta y = 0.004$	7.5947 (0.16 %)	-0.7398 (0.15 %)
$\Delta x = \Delta y = 0.002$	7.6072	-0.7409

Table 2. Results of grid-independent study; the values in parentheses denote percentage relative difference with respect to corresponding values of the minimum grid size case.

+10 throughout the paper. Also, quantitative values of the peak lift coefficient ( $C_L^{peak}$ ) and average drag coefficient ( $\bar{C}_D$ ) are presented in [table 1](#) along with the percentage relative difference with respect to the lowest  $\Delta t$  case considered. Both  $C_D$  and  $C_L$  time histories, as well as the vorticity contours, for  $\Delta t = 0.00005$  and  $0.0001$  are almost identical. Therefore,  $\Delta t = 0.0001$  is taken as the appropriate time step size for all the simulations hereafter.

### 2.3.2. Grid size convergence test

The optimal grid sizes  $\Delta x$  and  $\Delta y$  are also selected based on the outcomes of a grid independence study. To that end, different grid sizes,  $\Delta x = \Delta y = 0.002$ ,  $\Delta x = \Delta y = 0.004$  and  $\Delta x = \Delta y = 0.008$ , have been tested. The ratio of the stretching of the mesh towards the outer boundaries is kept the same, as mentioned in § 2.2, for all of these three different grid sizes. The time step size is taken as  $\Delta t = 0.0001$ , and the computational domain size is  $[-10.0, 30.0] \times [-12.5, 12.5]$  along the  $x$ - and  $y$ -axes, respectively. The quantitative values of  $C_L^{peak}$  and  $\bar{C}_D$ , and the percentage relative difference with respect to the lowest grid size case, are presented in [table 2](#). The time traces of  $C_D$  and  $C_L$ , as well as the vorticity contours, for grids  $\Delta x = \Delta y = 0.002$  and  $\Delta x = \Delta y = 0.004$  match very closely; see [figure 3](#). Hence the mesh corresponding to grid size  $\Delta x = \Delta y = 0.004$  is chosen for further simulations.

### 2.3.3. Domain size convergence test

The size of the computational domain is finalised after performing a domain independence test to ensure that the aerodynamic load coefficients do not change much with further increase in the domain size. Three different rectangular domains are chosen, with sizes as follows: ‘D1’,  $[-5.0, 15.0] \times [-6.25, 6.25]$ ; ‘D2’,  $[-10.0, 30.0] \times [-12.5, 12.5]$ ; and ‘D3’,  $[-20.0, 60.0] \times [-25.0, 25.0]$ ; with the pitching axis of the foil being placed at the origin at the start of simulations. Time step and minimum grid sizes are taken as  $\Delta t = 0.0001$  and  $\Delta x = \Delta y = 0.004$ , respectively, based on the outcomes of time and



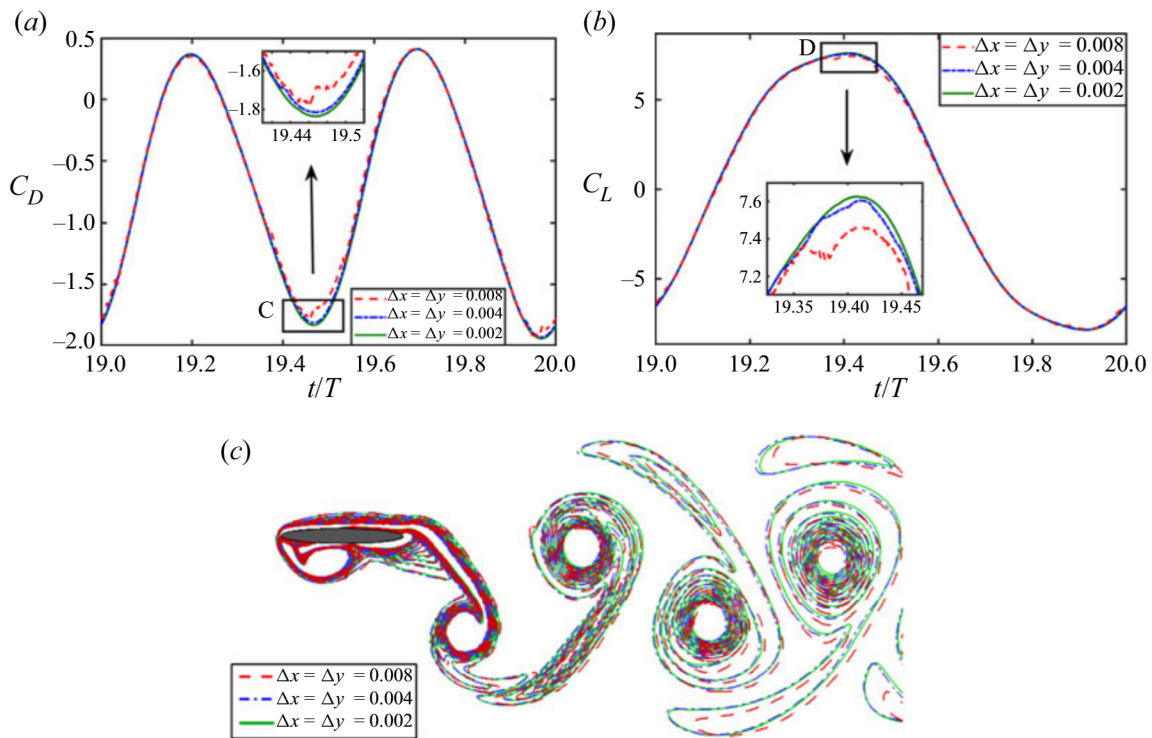


Figure 3. Grid independence test for the flow over a pitching–plunging foil: (a) drag and (b) lift coefficients, and (c) instantaneous vorticity contours at a typical time instant  $t/T = 20.25$ .

mesh convergence tests. Note here that the size of the dense zone and mesh-stretching common ratios are kept the same for all three domains. The  $C_L$  and  $C_D$  time histories and vorticity contour plot presented in figure 4 show that the results of the medium-sized domain D2 and largest domain D3 are almost identical and do not suffer from boundary effects. The same is evident from the percentage relative difference with respect to the largest domain size case as presented in table 3. Hence D2 is chosen to be the optimum size of the computational domain for all the following simulations.

### 3. Dynamical transitions in the flow field

A wide range of parametric variations has been considered in the present study to investigate their individual and combined effects on the flow field dynamics. This section starts with a description of the parametric space considered here. We also introduce the qualitative/quantitative tools used to distinguish the different nonlinear dynamical states of the flow field, and also demonstrate them for three representative cases of periodic, quasi-periodic and chaotic wakes, the three primary dynamical states encountered in the present study. Subsequently, the flow field behaviour under the entire range of parametric variations is discussed.

#### 3.1. The parametric space

It is known from our earlier studies that periodic-to-chaotic transition happens around  $\kappa h \geq 1.5$  (Badrinath *et al.* 2017; Bose & Sarkar 2018; Majumdar *et al.* 2020a; Bose *et al.* 2021). However, only the plunge amplitude was varied in those cases, focusing solely on the effects of this single parameter on the system dynamics. In contrast, the present study

Transition boundaries and an order-to-chaos map

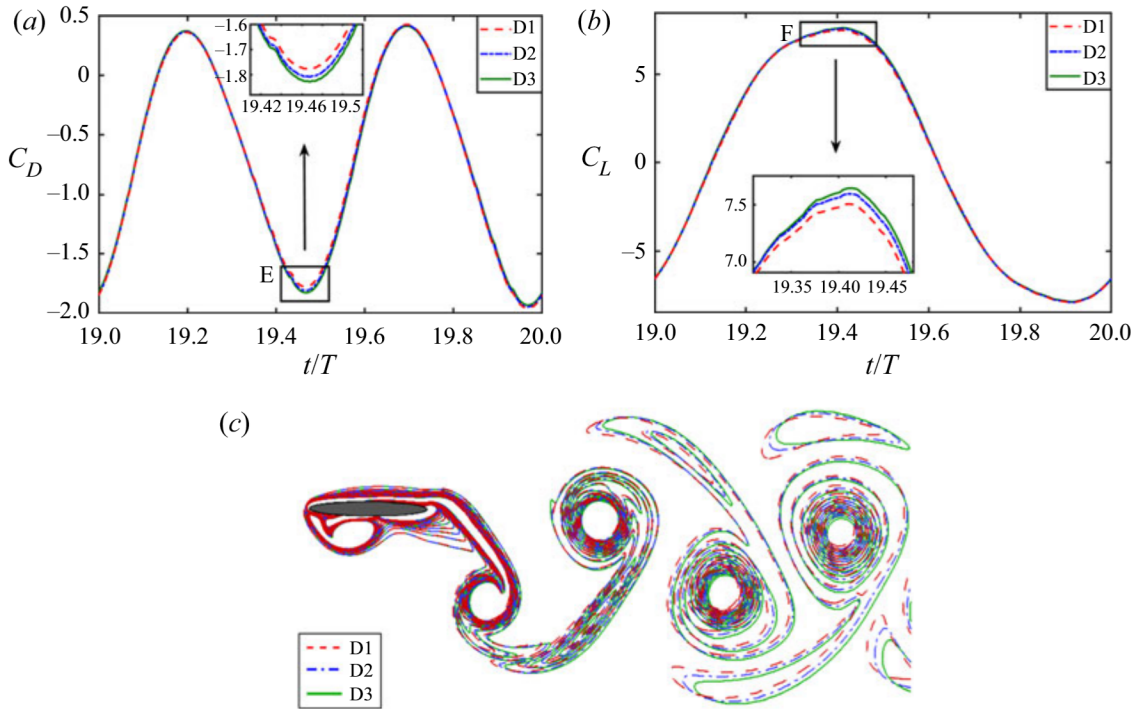


Figure 4. Domain size independence test for the flow over a pitching–plunging foil: (a) drag and (b) lift coefficients, and (c) instantaneous vorticity contours at a typical time instant  $t/T = 20.25$ .

Domain	Peak lift coefficient ( $C_L^{peak}$ )	Mean drag coefficient ( $\bar{C}_D$ )
D1: $[-5.0, 15.0] \times [-6.25, 6.25]$	7.5038 (1.40 %)	-0.7312 (1.69 %)
D2: $[-10.0, 30.0] \times [-12.5, 12.5]$	7.5947 (0.21 %)	-0.7398 (0.54 %)
D3: $[-20.0, 60.0] \times [-25.0, 25.0]$	7.6104	-0.7438

Table 3. Results of domain-size-independent study; the values in parentheses denote percentage relative difference with respect to corresponding values of the largest domain size case.

considers a much wider range of parametric variations for all the relevant key parameters, i.e. plunge amplitude ( $h = 0.25, 0.375, 0.475, 0.625$ ), pitch amplitude ( $\theta_0 = 5^\circ, 15^\circ, 25^\circ$ ), pitching axis location ( $x_0 = 0.25, 0.5, 0.75$ ), flapping frequency ( $\kappa = 2.0, 4.0, 8.0$ ) and phase offset (in the range  $0 \leq \phi \leq 2\pi$ , in steps of  $\pi/8$ ). Any of these kinematic parameters can potentially alter the near-field vortex interactions and affect the dynamical transition mechanisms in the flow field. Qualitatively different kinematics (sinusoidal and trapezoidal) are also included here, as well as different foil thickness to chord ratios ( $t_h/c = 0.06, 0.12, 0.18$ ). Throughout the study, the flow Reynolds number is kept constant at  $Re = 300$ . The overall parametric space is presented in table 4. Results for varying  $h$  and  $\phi$ , with  $\theta_0 = 15^\circ$ ,  $\kappa = 4.0$ ,  $x_0 = 0.5$  and  $t_h/c = 0.12$  being kept fixed, are presented first. The other parameters, i.e.  $\theta_0$ ,  $x_0$ ,  $\kappa$  and  $t_h/c$ , as well as the kinematic pattern, are varied next, one by one, keeping the rest of the parameters unchanged. For these cases, results are presented for plunge amplitude  $h = 0.475$  at four typically chosen phase offsets,  $\phi = \pi/2$ ,

Parameter	Values
Reynolds number	$Re = 300$
Non-dimensional plunge amplitude	$h = 0.25, 0.375, 0.475, 0.625$
Pitch amplitude	$\theta_0 = 5^\circ, 15^\circ, 25^\circ$
Mean pitch angle	$\theta_m = 0^\circ$
Pitching axis location	$x_0 = 0.25, 0.5, 0.75$
Reduced frequency	$\kappa = 2.0, 4.0, 8.0$
Phase offset between plunge and pitch motions	$\phi = \frac{\pi}{8}, \frac{2\pi}{8}, \frac{3\pi}{8}, \dots, 2\pi$
Thickness to chord ratio of the elliptic foil	$t_h/c = 0.06, 0.12, 0.18$

Table 4. The parameter space considered in the present study.

$\pi$ ,  $3\pi/2$  and  $2\pi$ . The above-mentioned different parametric combinations gave a total of 100 different simulation cases.

### 3.2. Measures used for dynamical characterisation of the flow field

The wake patterns are classified based on the dynamical characteristics of the unsteady flow field. When the evolution of the vortex structures repeats exactly in consecutive flapping cycles, the corresponding wake is classified as a periodic wake. On the other hand, in the quasi-periodic state, the flow field vortices do not overlap exactly after each cycle; instead, the positions of the vortex cores stay in the close neighbourhood of their previous cycle counterparts. The wake is classified as chaotic when the vortex structures never repeat and the long-term behaviour of the unsteady wake becomes completely unpredictable. These are the three main types of dynamics encountered in the present study. The dynamical states of the flow field at different parametric values are first identified qualitatively through the phase-averaged vorticity plots (Lentink *et al.* 2010), and subsequently confirmed quantitatively with the help of vorticity correlation values (Bose & Sarkar 2018) as well as the phase portraits and the Morlet wavelet transforms (Grossmann, Kronland-Martinet & Morlet 1990), which are presented in the supplementary material available at <https://doi.org/10.1017/jfm.2022.385>. Please note that the vorticity correlation coefficient values presented in this study are calculated as an average of the correlation coefficients obtained at the end of 16 consecutive flapping cycles (for  $t/T = 15.0$  to  $t/T = 30.0$ ). The phase-averaged vorticity plots are also obtained for the same number of flapping cycles. Since the flow field in the periodic regime repeats exactly, the average of the flow field data at the same time instant in several consecutive cycles gives a crisp image of the vorticity contour. But it gives a completely blurry image during chaos when there is no correlation between the flow fields in different cycles. However, the phase-averaged image is neither crisp nor entirely blurry in the quasi-periodic regime. The average vorticity correlation value ( $\rho$ ), if close to unity, represents periodicity, while it hovers near zero in the chaotic state denoting a near absence of correlation between the flow fields from different cycles. In the quasi-periodic regime, it stays between 0 and 1.

The dynamical characteristics are established further by using a series of other nonlinear time series tools from the dynamical systems theory, such as stroboscopic Poincaré sections (Hilborn *et al.* 2000), reconstructed phase portraits (Kennel, Brown & Abarbanel 1992) and recurrence plots (Marwan *et al.* 2007). The main advantage of these nonlinear time series tools is that they can establish the nature of the dynamics conclusively even

Transition boundaries and an order-to-chaos map

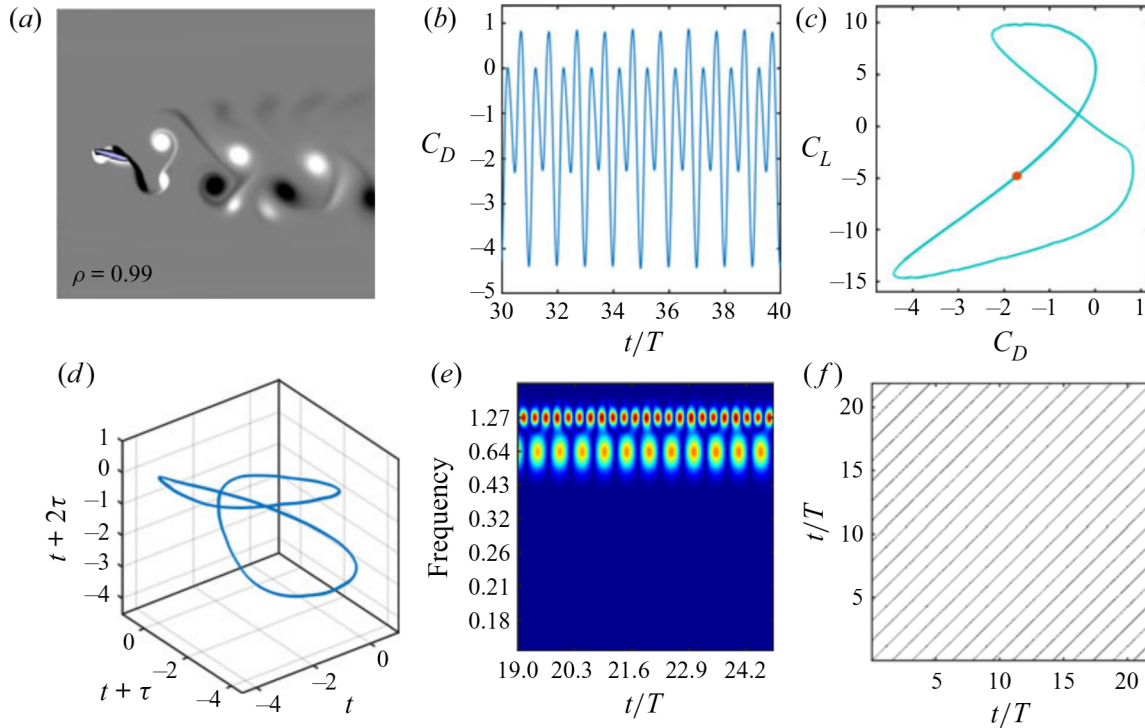


Figure 5. ‘Periodic dynamics’: (a) phase-averaged vorticity contour and average vorticity correlation; (b) time history of drag coefficient; (c)  $C_L-C_D$  phase portrait, where the corresponding stroboscopic Poincaré section (red dots) converges to a single point; (d) reconstructed phase portrait of  $C_D$ , depicting a close loop orbit; (e) organised narrow frequency band in Morlet wavelet transform; and (f) recurrence plot obtained from the reconstructed  $C_D$  data, displaying equidistant solid lines parallel to the main diagonal. All these measures indicate the signature of the periodic flow field. The parametric values are  $h = 0.475$ ,  $\theta_0 = 15^\circ$ ,  $\phi = 4\pi/8$ ,  $\kappa = 4.0$ ,  $x_0 = 0.5$  and  $t_h/c = 0.12$ .

with short time history data. This is particularly useful in our case as simulation of long time histories for many flapping cycles using a high-fidelity Navier–Stokes solver is associated with a prohibitive computational cost. The results obtained using these tools, along with the  $C_L-C_D$  phase portraits and Morlet wavelet transforms for three typically chosen parametric cases representative of the periodic, quasi-periodic and chaotic dynamics, are shown in figures 5–7, respectively. Note that these cases are selected randomly as representative cases, and the corresponding parametric values are mentioned in their respective figure captions. A closed loop orbit in the phase portrait diagram indicates a periodic dynamics. Here, the phase space trajectory repeats exactly in different cycles. Hence the stroboscopic Poincaré section converges to a single point (Hilborn *et al.* 2000). This is accompanied with an organised narrow frequency band on the wavelet transform plot, and equidistant solid lines parallel to the main diagonal on the recurrence plot. In contrast to periodic dynamics, the trajectory neither repeats exactly nor deviates significantly during the quasi-periodic state, but returns in the neighbourhood of its previous positions, eventually filling the phase space in the form of a toroidal shape, and the Poincaré section depicts a closed loop curve (Hilborn *et al.* 2000). The presence of modulating frequency bands along with incommensurate frequencies in the wavelet spectra and unequally spaced lines on the recurrence plot confirms quasi-periodicity. An irregular phase portrait with the Poincaré points being scattered, a broadband frequency

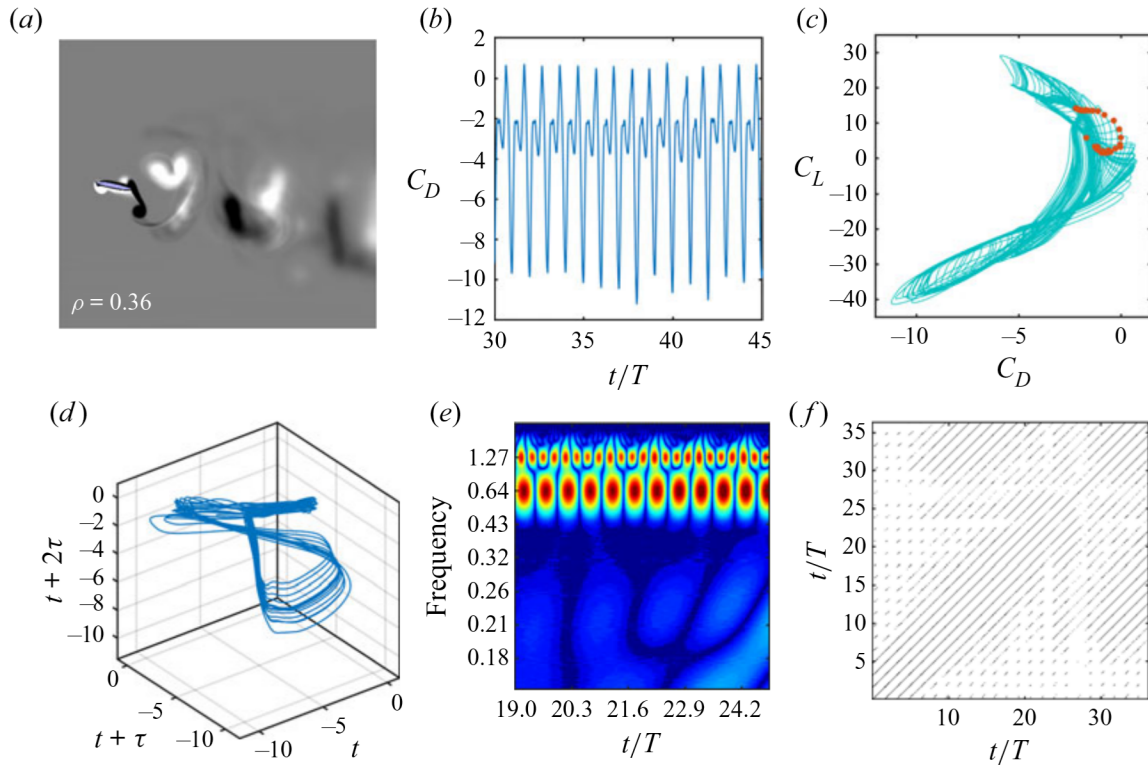


Figure 6. ‘Quasi-periodic dynamics’: (a) phase-averaged vorticity contour and average vorticity correlation; (b) time history of drag coefficient; (c)  $C_L - C_D$  phase portrait, where the corresponding stroboscopic Poincaré section (red dots) depicts a close loop; (d) reconstructed phase portrait of  $C_D$ , depicting a ‘toroidal’ phase portrait; (e) modulating incommensurate frequency band in Morlet wavelet transform; and (f) recurrence plot obtained from the reconstructed  $C_D$  data, displaying unequally spaced lines. All these measures indicate the signature of quasi-periodicity. The parametric values are  $h = 0.625$ ,  $\theta_0 = 15^\circ$ ,  $\phi = 6\pi/8$ ,  $\kappa = 4.0$ ,  $x_0 = 0.5$  and  $t_h/c = 0.12$ .

spectrum, short and broken diagonal lines along with isolated scattered points on the recurrence plot – all these confirm the existence of chaos in figure 7.

The above discussions demonstrate the way the flow field is classified dynamically in this study. The dynamical transition behaviour in the flow field under different parametric conditions is presented in the next subsection. Only the phase-averaged vorticity contours and the associated average vorticity correlation values are presented here, for the sake of brevity. The  $C_L - C_D$  phase portraits and the Morlet wavelet transforms are included in the supplementary material, and they are referred to in the paper in relevant discussions. Results of the other measures for all the 100 different parametric cases are not included here, for the sake of brevity.

### 3.3. Flow field behaviour under parametric variations

#### 3.3.1. Plunge amplitude ( $h$ ) and phase offset ( $\phi$ )

The dynamical transition observed by varying the plunge amplitude and phase offset is shown symbolically in figure 8. Here, each of the data points is marked according to the dynamical signature of the flow field observed in the simulations at those respective parameters. The periodic-to-chaotic transition in the flow field takes place through a quasi-periodic route. For  $\phi = \pi$ , the flow field is periodic for  $h \leq 0.375$ ; it exhibits a quasi-periodic behaviour at  $h = 0.475$ , and chaos at  $\kappa h = 0.625$  (figure 8). Note that

Transition boundaries and an order-to-chaos map

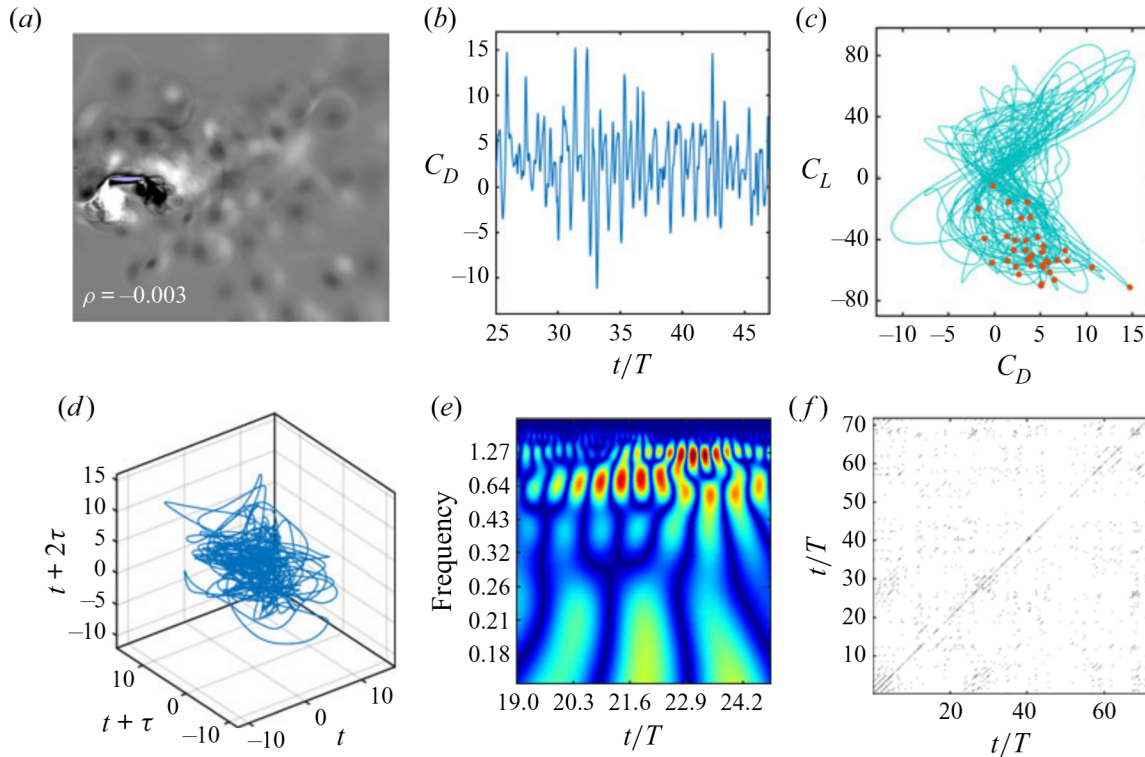


Figure 7. ‘Chaotic dynamics’: (a) phase-averaged vorticity contour and average vorticity correlation; (b) time history of drag coefficient; (c)  $C_L - C_D$  phase portrait, where the corresponding stroboscopic Poincaré section (red dots) is scattered; (d) reconstructed phase portrait of  $C_D$ , depicting a chaotic attractor; (e) broad banded frequency spectra in Morlet wavelet transform; and (f) recurrence plot obtained from the reconstructed  $C_D$  data, displaying short and broken diagonal lines along with isolated scattered points. All these measures indicate the signature of chaos. The parametric values are  $h = 0.625$ ,  $\theta_0 = 15^\circ$ ,  $\phi = 2\pi$ ,  $\kappa = 4.0$ ,  $x_0 = 0.5$  and  $t_h/c = 0.12$ .

with the variation in  $\phi$ , the onset of the transition along  $h$  changes significantly, though the qualitative route remains unchanged. For  $2\pi/8 \leq \phi \leq 6\pi/8$ , the flow field remains periodic even for higher  $h$  ( $h = 0.475$ ) (figure 8), whereas it becomes chaotic even at lower  $h$  values ( $h = 0.375$ ) for  $3\pi/2 \leq \phi \leq 2\pi$  (figure 8). Thus aperiodic onset gets advanced or delayed depending on the phase offset. This can be attributed to the LEV separation behaviour, which is strongly dependent on  $\phi$ , as will be discussed in § 4. The flow field results supporting the dynamical transition and the variety in the trailing-wake behaviour are shown in figures 9 and 10. Phase-averaged wake images and average vorticity correlation values are presented for different  $\phi$  cases in steps of  $2\pi/8$ .

**$h = 0.25$ :** Figure 8 reveals that for  $h = 0.25$ , a periodic pattern is shown by the wake for almost all  $\phi$  values, except for  $11\pi/8$  to  $13\pi/8$ , where it turns quasi-periodic. For  $h = 0.25$ , clockwise (CW) and counter-clockwise (CCW) vortices are seen to shed alternatively in each flapping cycle from the trailing edge. A drag-producing von Kármán wake is observed at  $\phi = 2\pi/8$  (figure 9a), and a reverse von Kármán wake is seen for  $3\pi/8 \leq \phi \leq 10\pi/8$ . The flow remains completely attached to the body without any LEV formation (figures 9b–e). For  $2\pi/8 \leq \phi \leq 10\pi/8$ , the flow field is periodic and repeats exactly, as revealed by the crisp phase-averaged images. The vorticity correlation remains very close to unity, signifying a strong correlation between the flow fields of different cycles. However, for the  $\phi = 12\pi/8$  case, the phase-averaged contour is neither crisp nor entirely blurry (figure 9f). The correlation value comes down to 0.74, indicating a

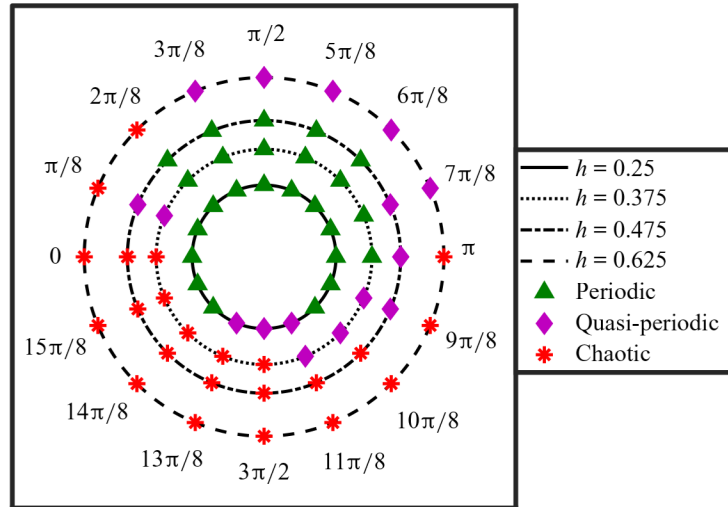


Figure 8. Summarising the dynamical states observed at different  $h$  and  $\phi$  values, keeping other parameters fixed.

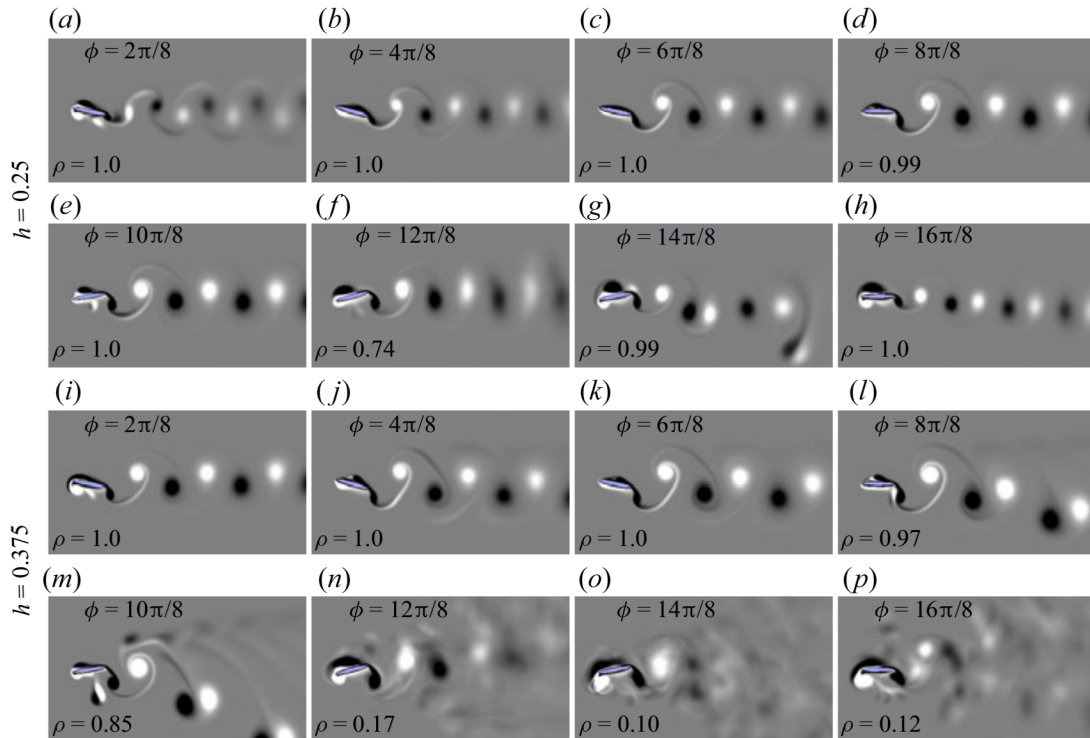


Figure 9. Phase-averaged vorticity contours at different  $\phi$ : (a–h)  $h = 0.25$ , and (i–p)  $h = 0.375$ .

quasi-periodic flow signature. The flow field returns to periodicity at  $14\pi/8 \leq \phi \leq 2\pi$  (figures 9g,h). The  $C_L-C_D$  phase portraits and the wavelet spectra of all the above cases are presented, respectively, in figures 1(a–h) and 3(a–h) of the supplementary material.

**$h = 0.375$ :** For  $\phi = 2\pi/8$ , the von Kármán wake of  $h = 0.25$  turns into reverse von Kármán at  $h = 0.375$  (figure 9i). The wake undergoes deflection during  $4\pi/8 \leq \phi \leq 10\pi/8$ , and the deflection angle increases with the increase in  $\phi$ ; see figures 9(j–m). The flow remains periodic in the range  $2\pi/8 \leq \phi \leq 8\pi/8$ , but shows quasi-periodic signatures at  $\phi = 10\pi/8$  with  $\rho = 0.85$ . The flow field exhibits chaos for  $12\pi/8 \leq \phi \leq 2\pi$ , where

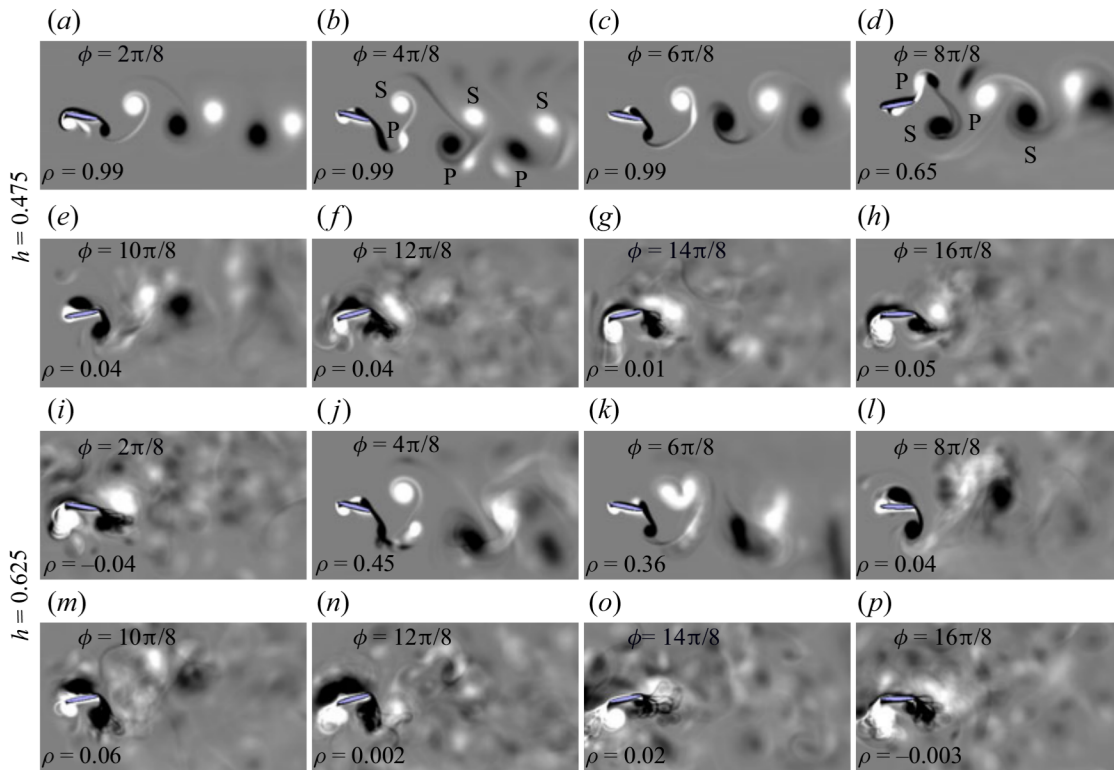


Figure 10. Phase-averaged vorticity contours at different  $\phi$ ; (a–h)  $h = 0.475$ , and (i–p)  $h = 0.625$ .

the flow is irregular and the long-term behaviour is unpredictable. Chaos is confirmed by the correlation values being close to zero, and also the entirely blurry patterns seen in figures 9(n–p). The phase portrait and wavelet plots corresponding to the cases of figures 9(i–p) are presented in figures 1(i–p) and 3(i–p) of the supplementary material, respectively, and support the dynamical characteristics observed in the flow field plots.

**$h = 0.475$ :** At this  $h$ , the trailing wake exhibits several interesting flow patterns for varying  $\phi$ . A deflected reverse von Kármán wake is seen at  $\phi = 2\pi/8$  (figure 10a), with CW and CCW vortices shed in alternate fashion at every cycle. An S + P pattern (Williamson & Roshko 1988) is seen at  $\phi = 4\pi/8$  (figure 10b) with a single CCW vortex (S) and a pair of CW and CCW vortices (P) shed in every cycle. For the latter, the CCW part of P gets shredded (Gustafson & Leben 1988) gradually under the influence of its stronger CW partner, and the far wake transforms to a downward deflected reverse von Kármán wake. The deflection direction gets reversed as  $\phi$  crosses  $\pi/2$ , giving an upward deflected wake at  $\phi = 6\pi/8$  (figure 10c). This is because the initial direction of the pitch rotation gets reversed as  $\phi$  crosses  $\pi/2$ , influencing the direction of deflection (Zheng & Wei 2012; Majumdar, Bose & Sarkar 2020b). Although the wake patterns vary with  $\phi$ , they remain periodic within  $2\pi/8 \leq \phi \leq 6\pi/8$ , and turn quasi-periodic at  $\phi = 8\pi/8$  (figure 10d). Finally, the flow field becomes chaotic for  $10\pi/8 \leq \phi \leq 2\pi$  as denoted by the entirely blurry phase-averaged patterns and almost zero vorticity correlation; see figures 10(e–h). Figures 2(a–h) and 4(a–h) of the supplementary material present the phase portrait and wavelet plots corresponding to the cases of figures 10(a–h), respectively.

**$h = 0.625$ :** At this high plunge amplitude, the organised pattern of the wake is almost entirely lost, and chaos is seen for a wide range of  $\phi$  ( $0 \leq \phi \leq 2\pi/8$  and  $\pi \leq \phi \leq 2\pi$ ); see figures 10(i,l–p). Outside this regime ( $3\pi/8 \leq \phi \leq 7\pi/8$ ), quasi-periodic flow signatures



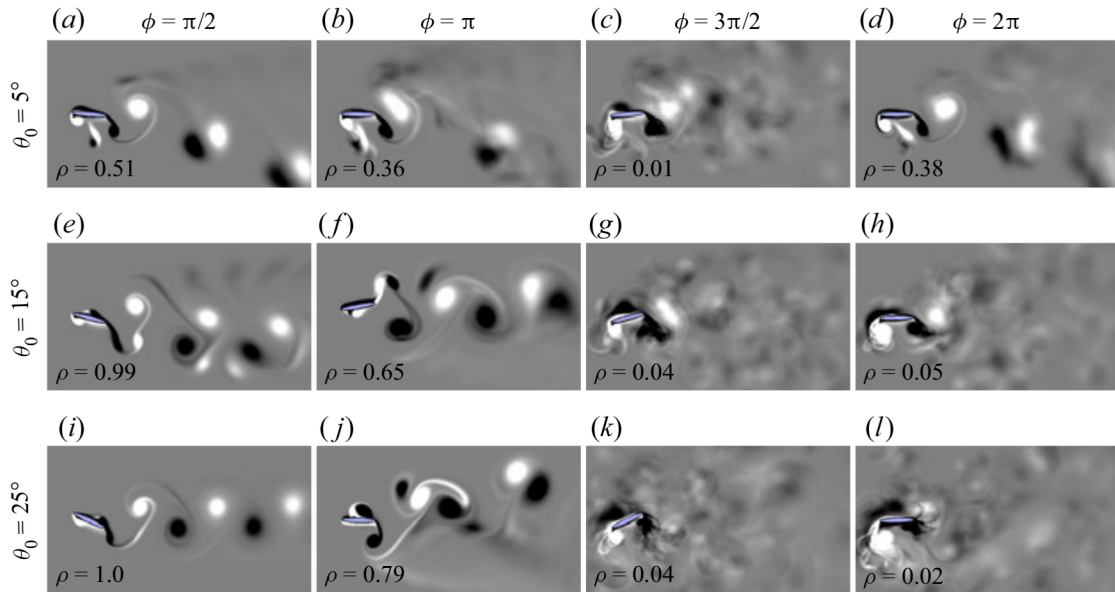


Figure 11. Phase-averaged vorticity contours for different pitch amplitudes and phase offsets at  $h = 0.475$ ,  $\kappa = 4.0$ ,  $x_0 = 0.5$  and  $t_h/c = 0.12$ .

are observed (figures 10j,k). These claims are confirmed further by the  $C_L-C_D$  phase portraits and wavelet spectra presented in figures 2(i-p) and 4(i-p) of the supplementary material.

### 3.3.2. Pitch amplitude, $\theta_0$

The pitch amplitude is varied as  $\theta_0 = 5^\circ$ ,  $15^\circ$  and  $25^\circ$ . Other kinematic parameters are kept fixed at  $h = 0.475$ ,  $\kappa = 4.0$ ,  $x_0 = 0.5$  and  $t_h/c = 0.12$ . Figure 11 presents the dynamical states corresponding to these parametric cases, and the identified dynamical signatures are further confirmed by  $C_L-C_D$  phase plots and wavelet spectra presented in figures 5 and 6 of the supplementary material. For  $\theta_0 = 15^\circ$  and  $25^\circ$ , the transition route remains the same, i.e. periodic at  $\phi = \pi/2$ , quasi-periodic at  $\phi = \pi$ , and chaos at  $\phi = 3\pi/2$  and  $2\pi$ . At  $\theta_0 = 5^\circ$ , the effect of the pitch motion is comparatively lesser, with the flow field getting dictated primarily by the dominant plunge motion. For this  $\theta_0$ , the periodic flow field is absent at the chosen  $\phi$  values; quasi-periodic flow is seen for  $\phi = \pi/2$ ,  $\pi$  and  $2\pi$ ; and robust chaos is exhibited at  $\phi = 3\pi/2$ .

### 3.3.3. Location of the pitching axis, $x_0$

To investigate the effect of different pitching axis locations, three different pivot points have been chosen,  $x_0 = 0.25$ ,  $0.5$  and  $0.75$ , i.e. at the quarter-chord, mid-chord and three-quarter-chord, respectively. All other parameters are kept fixed at  $h = 0.475$ ,  $\theta_0 = 15^\circ$ ,  $\kappa = 4.0$  and  $t_h/c = 0.12$ . The resulting flow field dynamics are demonstrated in figure 12. The corresponding  $C_L-C_D$  phase portraits and wavelet transforms of  $C_D$  time histories are presented in figures 7 and 8 of the supplementary material, respectively. It is evident from these results that the dynamical states are not drastically different for different pitching axis locations. The influence of pivot location on the dynamical characteristics is insignificant at  $\phi = \pi/2$  and  $3\pi/2$ . The flow field displays periodicity at  $\phi = \pi/2$ , and chaos at  $\phi = 3\pi/2$ . However at  $\phi = \pi$ , there is gradual change in the dynamical signature,

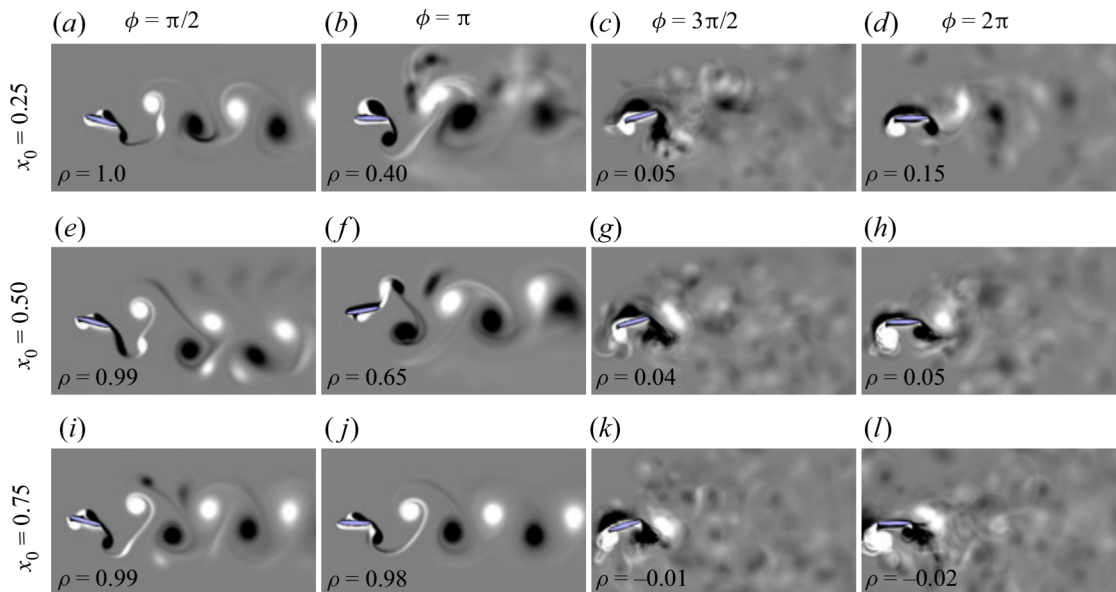


Figure 12. Phase-averaged vorticity contours for different pitching axis locations and phase offsets at  $h = 0.475$ ,  $\theta_0 = 15^\circ$ ,  $\kappa = 4.0$  and  $t_h/c = 0.12$ .

showing quasi-periodicity for  $x_0 = 0.25$  and  $x_0 = 0.5$ , but purely periodic behaviour at  $x_0 = 0.75$ . This indicates that the flow field gets regularised gradually as the pivot location is moved towards the trailing edge at  $\phi = \pi$ . This can be noticed from the gradual increase in the average vorticity correlation values at  $\phi = \pi$  ( $\rho = 0.40, 0.65$  and  $0.98$  at  $x_0 = 0.25, 0.5$  and  $0.75$ , respectively); see [figure 12](#). On the other hand, at  $\phi = 2\pi$ , despite all three  $x_0$  cases being chaotic, an increase in the degree of irregularity can be noticed from the decrease in the magnitude of average vorticity correlation values as  $x_0$  increases ( $|\rho| = 0.15, 0.05$  and  $0.02$  at  $x_0 = 0.25, 0.5$  and  $0.75$ , respectively); see [figure 12](#). In conclusion, as the pivot point is moved from the leading edge towards the trailing edge, the flow field gets regularised at  $\phi = \pi$ , but becomes more and more irregular at  $\phi = 2\pi$ . The physical reason behind this trend is presented in [Appendix C](#), as this can be appreciated better after the discussion on the role of flapping motion on LEV growth, and in turn, on the dynamical states, as given in §§ 4 and 5.1.

### 3.3.4. Flapping frequency, $\kappa$

In this case, we have chosen two new flapping frequencies,  $\kappa = 2.0$  and  $8.0$ , i.e. half of and double the earlier chosen frequency. Other kinematic parameters are kept fixed at  $h = 0.475$ ,  $\theta_0 = 15^\circ$ ,  $x_0 = 0.5$  and  $t_h/c = 0.12$ . The phase-averaged vorticity contour plots are presented in [figure 13](#). Figures 9 and 10 of the supplementary material present the corresponding  $C_L - C_D$  phase plots and the wavelet spectra, respectively. For  $\kappa = 2.0$ , the resultant dynamical flapping velocity is so low that the flow exhibits a periodic dynamic independent of the phase offset value between pitch and plunge motions. On the other hand, at  $\kappa = 8.0$ , the flapping velocity being significantly high, the flow field exhibits chaos at all  $\phi$  values. Thus the flapping frequency can be a control parameter to trigger a periodic to chaotic transition in the wake.

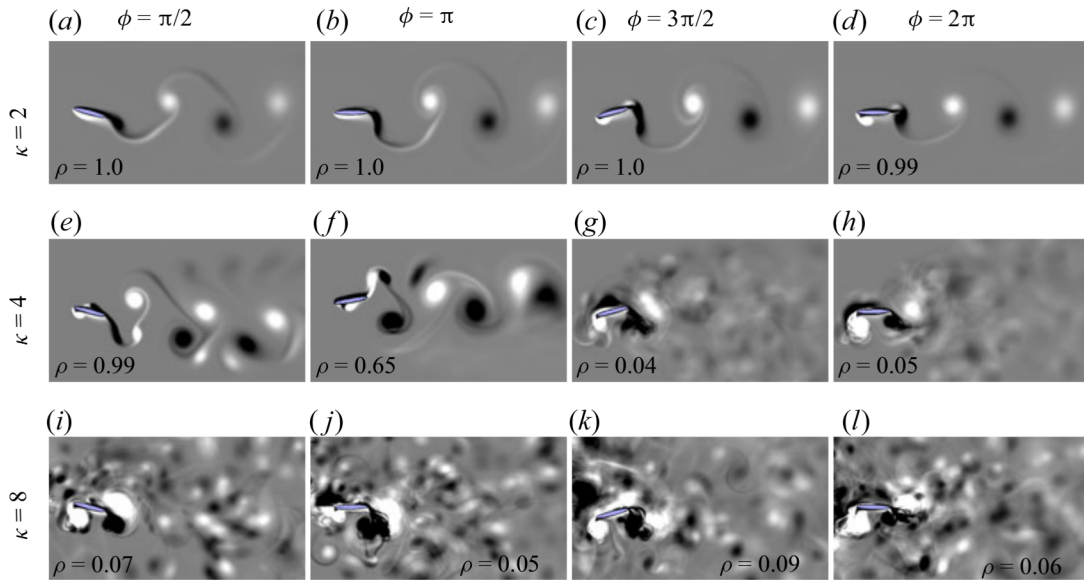


Figure 13. Phase-averaged vorticity contours for different flapping frequencies and phase offsets at  $h = 0.475$ ,  $\theta_0 = 15^\circ$ ,  $x_0 = 0.5$  and  $t_h/c = 0.12$ .

### 3.3.5. Thickness to chord ratio of the foil, $t_h/c$

The simulations are run for different foil thicknesses with three different thickness to chord ratios,  $t_h/c = 0.06$ ,  $0.12$  and  $0.18$ , respectively, keeping the kinematic parameters constant at  $h = 0.475$ ,  $\theta_0 = 15^\circ$ ,  $\kappa = 2.0$  and  $x_0 = 0.5$ . The phase-averaged vorticity contours shown in figure 14 display clearly that the dynamical states for the three chosen foil thicknesses remain almost the same – periodic at  $\phi = \pi/2$ , quasi-periodic at  $\pi$  and chaotic at  $3\pi/2$ , respectively. However, a minor difference is observed at  $\phi = 2\pi$ , where  $t_h/c = 0.06$  and  $t_h/c = 0.12$  result in chaos, while the thicker foil with  $t_h/c = 0.18$  exhibits quasi-periodicity. Though the flow dynamics is quasi-periodic at  $t_h/c = 0.18$ , the average correlation of the vorticity field remains on the lower side ( $\rho = 0.23$ ). This signifies that the system at this parametric situation is very close to chaos, and any small change in the parameters may push it to robust chaos. It can be concluded here that the foil shape does not play a crucial role behind transition under the chosen parametric conditions. The dynamical characteristics remain more or less similar irrespective of the change in the thickness or shape, provided that the foil is not significantly thick ( $t_h/c = 0.18$  or greater based on the observations of the present study).

### 3.3.6. Flapping profile

The discussion so far has been based entirely on pure sinusoidal kinematics, and will be referred to as ‘Flapping I’ hereafter. In this section, another variety of flapping motion pattern is tested, namely a sinusoidal plunge along with a trapezoidal pitch motion, and this will be referred to as ‘Flapping II’ in this study. The kinematics is given by

$$y_p(t) = h_0 \sin(2\pi f_e t), \quad (3.1)$$

$$\theta(t) = \theta_m + \frac{\theta_0}{\tanh \beta} \tanh(\beta \sin(2\pi f_e t + \phi)), \quad (3.2)$$

where  $\beta$  is a scaling parameter to match the amplitudes, taken as  $\beta = 2.5$  in this study.

Transition boundaries and an order-to-chaos map

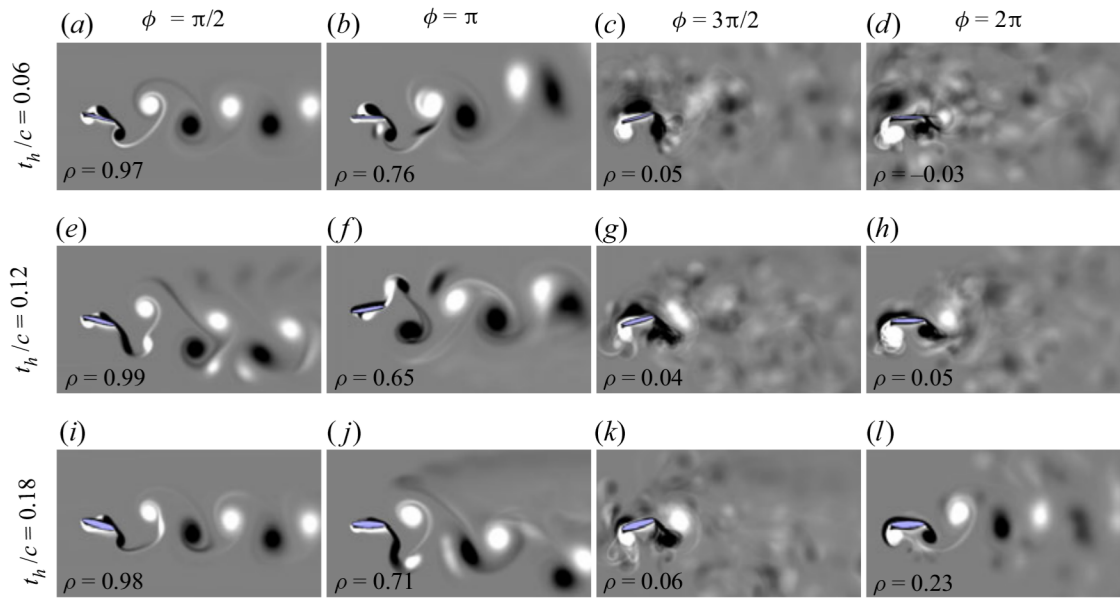


Figure 14. Phase-averaged vorticity contours for different foil thicknesses and phase offsets at  $h = 0.475$ ,  $\theta_0 = 15^\circ$ ,  $\kappa = 4.0$  and  $x_0 = 0.5$ .

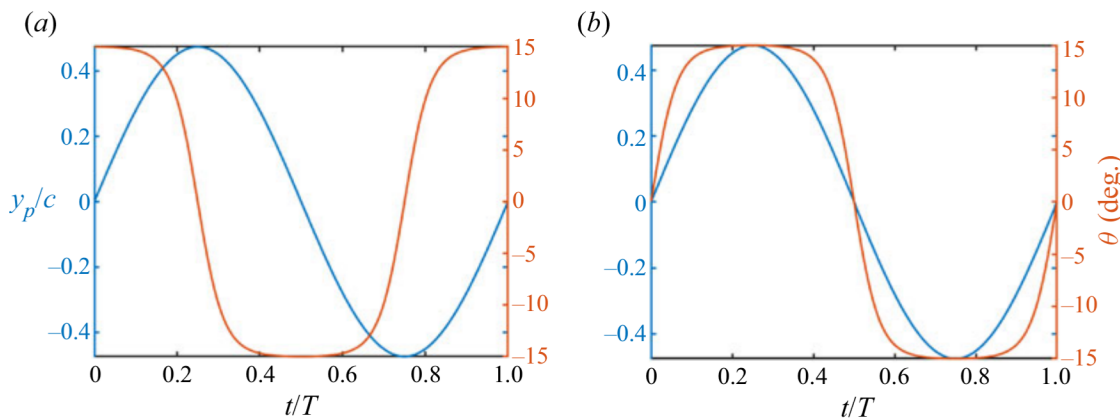


Figure 15. Flapping pattern considering sinusoidal plunge along with trapezoidal pitch motion: (a)  $\phi = \pi/2$ , and (b)  $\phi = 2\pi$ .

The kinematic parameters are taken as  $h = 0.475$ ,  $\theta_0 = 15^\circ$ ,  $\kappa = 4.0$ ,  $x_0 = 0.5$  and  $t_h/c = 0.12$ . Once again, four different  $\phi$  values are chosen,  $\phi = \pi/2$ ,  $\pi$ ,  $3\pi/2$  and  $2\pi$ . Figure 15 shows the flapping patterns for  $\phi = \pi/2$  and  $2\pi$ . The dynamical states of the flow fields are presented in figure 16; the  $C_L-C_D$  plots and wavelet transforms are given in figures 13 and 14 of the supplementary material. It is seen that the transition route remains the same for both Flapping I and Flapping II, exhibiting periodicity at  $\phi = \pi/2$ , quasi-periodicity at  $\phi = \pi$ , and chaos at  $\phi = 3\pi/2$  and  $2\pi$ . This indicates that small changes in the flapping pattern do not affect the dynamical transition behaviour much.

With the knowledge of the dynamics from these 100 different simulation cases, the role of the key vortex structures, especially the LEV, in triggering aperiodicity in the wake is investigated next. A correlation between the strength of the LEV and the dynamical state of the wake is also sought.

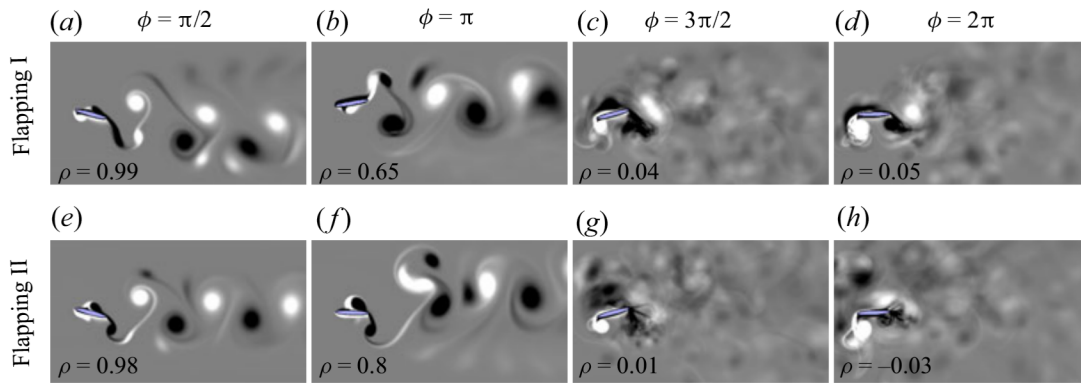


Figure 16. Phase-averaged vorticity contours for different flapping patterns and phase offsets at  $h = 0.475$ ,  $\theta_0 = 15^\circ$ ,  $\kappa = 4.0$ ,  $x_0 = 0.5$  and  $t_n/c = 0.12$ . Flapping I: sinusoidal plunge and sinusoidal pitch. Flapping II: sinusoidal plunge and trapezoidal pitch.

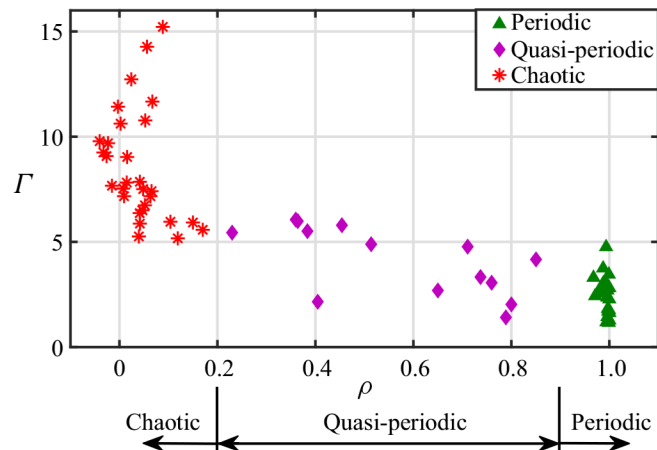


Figure 17. Average circulation of the primary LEV shows strong correlation with the periodicity of the flow field.

#### 4. Role of the primary LEV on flow field periodicity

The primary LEV is one of the key near-field structures to dictate the dynamical state of the flow field. As mentioned in the Introduction, LEV growth and separation become aperiodic in the high  $\kappa h$  regime, and the subsequent LEV–TEV interactions lead to spontaneous formation and destruction of series of secondary vortices, thus triggering aperiodicity in the wake (Bose & Sarkar 2018; Majumdar *et al.* 2020a; Bose *et al.* 2021). The strong interconnection between LEV growth and the chaotic transition of the flow field is demonstrated quantitatively in the present study in terms of the strength of the LEV. Figure 17 shows the variation in the average LEV strength ( $\Gamma$ ) at different parametric cases, along with the associated  $\rho$  values, presented in § 3.3. In order to estimate the LEV strengths, circulation values are calculated as an integral of the vorticity field over a rectangular region that covers the LEV area around the location of maximum vorticity (Zurman-Nasution *et al.* 2020). The position and size of the rectangular box are changed depending on the location and size of the primary LEV at different time instants and different parameters. Some examples of such rectangular regions surrounding the LEV can be seen in figure 18 for a few typical flow field snapshots. The integration is performed at a time instant when the foil completes an upstroke and reaches its topmost position.

Transition boundaries and an order-to-chaos map

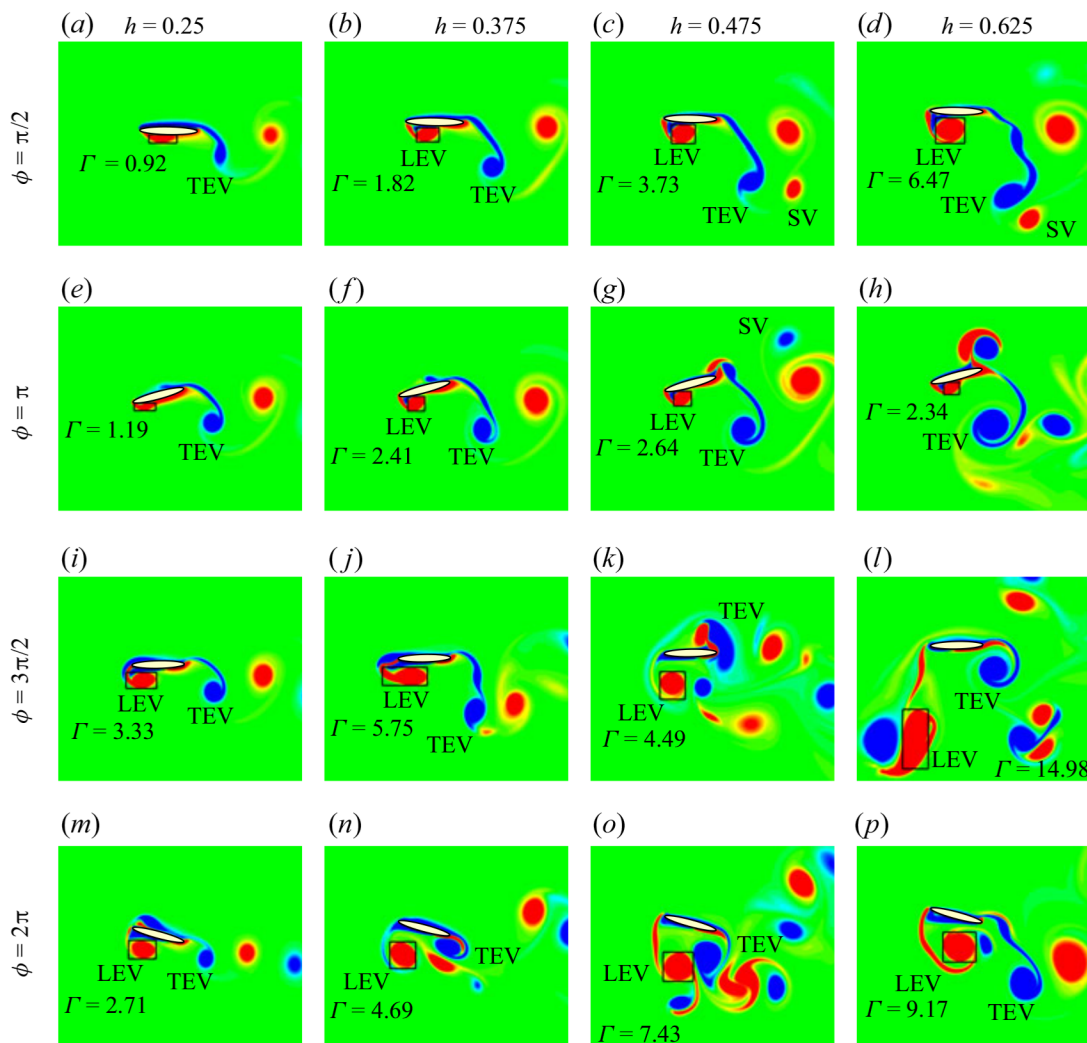


Figure 18. Comparison of the instantaneous vorticity contours at  $t/T = 20.25$  (at the end of an upstroke) for  $h = 0.25, 0.375, 0.475, 0.625$  at four typically chosen phase offset values ( $\phi = \pi/2, \pi, 3\pi/2, 2\pi$ ). The circulation of the primary LEV is mentioned in each panel. The black rectangular boxes show the region considered to calculate the circulation values. SV: secondary vortex.

The primary counter-clockwise LEV is assumed to be fully grown at this instant. The LEV circulation is obtained for 16 consecutive flapping cycles ( $t/T = 15-30$ ), and the average LEV strength,  $\Gamma$ , is computed. From the  $\Gamma$  versus  $\rho$  plot in figure 17, a direct correlation between the strength of the primary LEV and the chaotic transition in the flow field can be observed. For the periodic cases, in general,  $\Gamma$  is seen to remain bounded (approximately  $\Gamma < 5$ ). In the majority of these cases, the LEV, being weak in strength, does not get shed and remains attached to the body. As a result, no LEV–TEV interactions take place in the near field. For the quasi-periodic cases,  $\Gamma$  is seen to cover almost the same range as that of the periodic cases (approximately  $1.5 < \Gamma < 6$ ). So periodic and quasi-periodic dynamics cannot be distinguished clearly based on the  $\Gamma$  values alone. On the other hand, for most of the chaotic cases,  $\Gamma$  goes beyond a certain threshold, approximately at  $\Gamma > 6$ ; see figure 17. This indicates that beyond a certain strength, the growth of the LEV turns chaotic, triggering the entire flow field to be chaotic eventually. Notably large variations in the circulation values at different cycles are seen during chaos, and a high

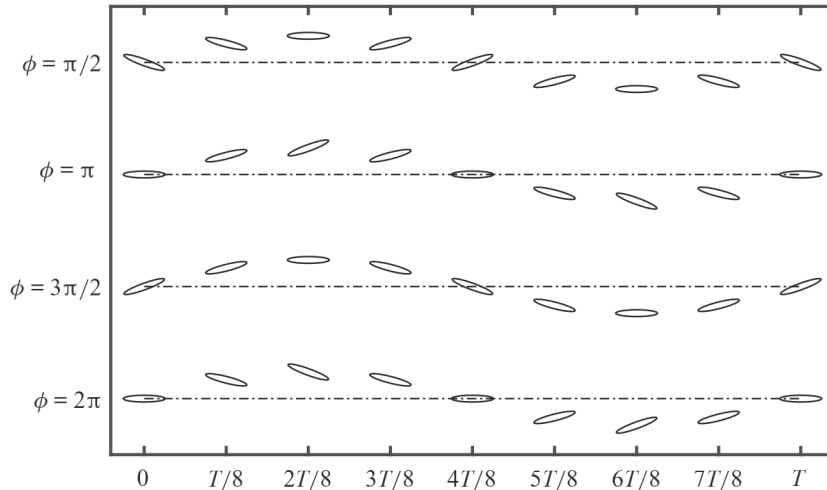


Figure 19. Schematic diagram showing the pitching–plunging foil motion at  $\phi = \frac{\pi}{2}, \pi, \frac{3\pi}{2}$  and  $2\pi$ .

average is observed. A strong LEV is shed from the body during different flapping cycles aperiodically, and subsequently interacts with the TEV to propagate chaos in the wake.

The fundamental mechanisms that dictate the onset of chaotic transition are related to the LEV and other near-field vortices, as will be shown next. They are examined in this section based on a few typically chosen representative cases. A comparison of the near-field vortices at four  $h$  values (0.25, 0.375, 0.475, 0.625) is presented in figure 18 for four typical  $\phi$  cases ( $\pi/2, \pi, 3\pi/2, 2\pi$ ). These representative cases are taken from § 3.3.1. Note that the circulation values shown in the panels of figure 18 correspond to each specific snapshot, and are not the averaged quantities. For a better appreciation of the foil motion, the orientations of the foil at different time instants during a flapping cycle are shown schematically in figure 19, corresponding to the cases presented in figure 18. These pictorial representations will be useful in the follow-up discussion. The effective AoA  $\alpha_{eff}$  is also computed for each of these cases using the equation

$$\alpha_{eff}(t) = \theta(t) - \tan^{-1} \left[ \frac{1}{U_\infty} \left\{ \dot{y}_p(t) - \left( \frac{c}{2} - x_0 \right) \dot{\theta}(t) \cos(\theta(t)) \right\} \right]. \quad (4.1)$$

The derivation of this equation is given in Appendix A. The numerical value of  $\alpha_{eff}$  depends on both the plunge and pitch parameters, as well as on the phase offset between them. Figure 20 presents  $\alpha_{eff}$  over a flapping cycle for a typical case with  $h = 0.475$  at four different  $\phi$  values. The trend remains the same for the other  $h$  values. The  $\alpha_{eff}$  values reported in the following discussion are specific to the  $h = 0.475$  case.

The phase offset between the plunge and pitch motions is a crucial parameter in ultimately dictating the relative orientation of the flapping foil with respect to the incoming flow. At  $\phi = \pi/2$ , the leading edge of the foil leads the trailing edge, and the foil ‘slices through’ the free stream (see figure 19), thus minimising the maximum value that the effective AoA can reach ( $\alpha_{eff}^{max} = 47.24^\circ$  for  $h = 0.475$ , see figure 20). As a result, the flow remains completely attached to the body at  $h = 0.25$  (figure 18a). Even though an LEV forms with an increase in  $h$ , the circulation of the LEV remains low ( $\Gamma = 1.82$  at  $h = 0.375$ , and  $\Gamma = 3.73$  at  $h = 0.475$ ), and it stays attached to the body. No strong LEV separation is seen. The LEV does not undergo any direct interaction with the TEV; see figures 18(b,c). Thus for  $\phi = \pi/2$ , the flow field exhibits periodic vortex shedding

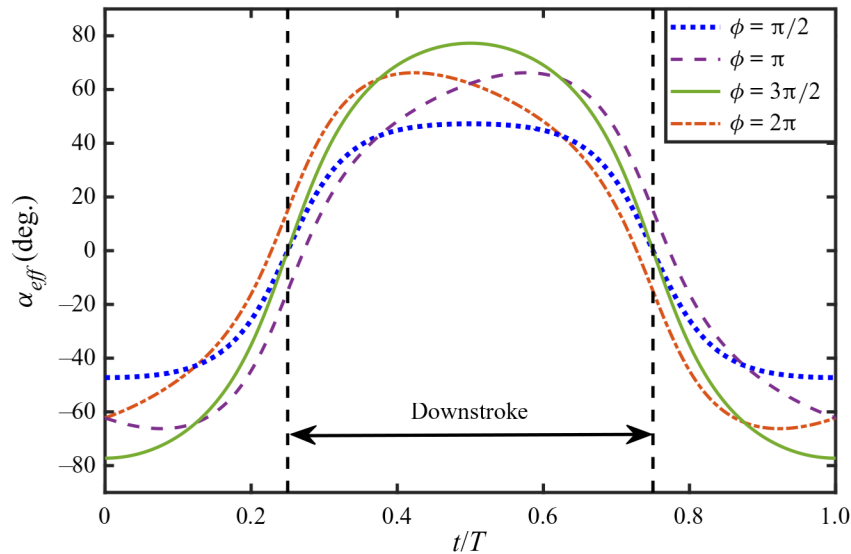


Figure 20. Effective AoA for a typical case  $h = 0.475$  at four different  $\phi$  values. The trend remains the same at the other  $h$  values.

even at  $h = 0.475$ . The periodic formation and growth of the primary LEV becomes quasi-periodic only at a significantly high  $h = 0.625$ , when the circulation of the primary LEV also increases to  $\Gamma = 6.47$ .

As  $\phi$  goes to  $\pi$ , the flow still remains attached at  $h = 0.25$ , and periodic vortex shedding is seen at the trailing edge (figure 18e). With an increase in  $h$ , an LEV forms as seen in figures 18(f–h). At this  $\phi$ , although the maximum effective AoA is high ( $\alpha_{eff}^{max} = 66.24^\circ$  for  $h = 0.475$ , as in figure 20), the leading edge traverses the smallest distance. Hence the LEV does not get separated from the body. However, it gradually gets convected along the foil surface to affect the TEV shedding. As the LEV growth becomes aperiodic around  $h \geq 0.475$ , it triggers the entire near-field interactions to be aperiodic.

At  $\phi = 3\pi/2$ , the kinematics being exactly the mirror image of those for  $\phi = \pi/2$ , the leading edge lags the trailing edge (figure 19), and  $\alpha_{eff}^{max}$  takes the highest value among all the other  $\phi$  cases ( $\alpha_{eff}^{max} = 77.24^\circ$  for  $h = 0.475$ , see figure 20). As a result, strong separation happens near the leading edge (figures 18i–l) and it becomes aperiodic even near  $h = 0.25$ . The aperiodically shed LEV (with  $\Gamma = 5.75$  at  $h = 0.375$ ,  $\Gamma = 4.49$  at  $h = 0.475$ , and  $\Gamma = 14.98$  at  $h = 0.625$ ), interacts with the TEV to trigger chaos. Consequently, spontaneous formation and annihilation of vortices through some of the fundamental interaction mechanisms sustains chaos in the far wake. Such interaction mechanisms were discussed in detail by Bose & Sarkar (2018) and Majumdar *et al.* (2020a).

At  $\phi = 2\pi$ , plunge and pitch are in the same phase, and the leading edge traverses the largest distance, giving a high maximum effective AoA ( $\alpha_{eff}^{max} = 66.24^\circ$  for  $h = 0.475$ , see figure 20). A strong LEV gets separated even at low  $h$ , but with high LEV strength. This can be seen from figures 18(n–p) ( $\Gamma = 2.71$  at  $h = 0.25$ ,  $\Gamma = 4.69$  at  $h = 0.375$ ,  $\Gamma = 7.43$  at  $h = 0.475$ , and  $\Gamma = 9.17$  at  $h = 0.625$ ). Once again, subsequent interactions with the TEV usher in and sustain chaos.

The above discussion underlines the importance of the foil orientation in affecting the growth and evolution of the primary LEV and in dictating its subsequent interactions with the other vortices. Parameters such as the phase offset can influence this strongly. One can



state from the above results that the  $\phi = \pi/2$  case should be preferred for a delayed onset of chaos as it ensures no strong separation and an organised flow for a longer range of  $h$ . Similarly,  $3\pi/2 \leq \phi \leq 2\pi$  should be avoided as the aperiodic onset gets advanced due to the formation and shedding of strong aperiodic leading-edge vortices, even at low  $h$ .

At this juncture, it is important to identify new non-dimensional parameters that can capture robustly the combined effects of the key kinematics on the LEV separation behaviour discussed above. These novel non-dimensional parameters are to be utilised to demarcate the different dynamical states of the wake without any loss of generality. With this focus, the next section identifies two new non-dimensional parameters and proposes a mathematical fit in terms of them to isolate the order-to-chaos transition region and classify the dynamical states.

## 5. Dynamical transition boundaries and an order-to-chaos map

As already mentioned, none of the conventionally used existing non-dimensional parameters ( $\kappa h$ ,  $St_A$ ,  $St_D$ ,  $St_c$ ,  $St_\tau$ ) can account for the combined effect of many different kinematic quantities. The limitations of the earlier approaches using existing non-dimensional parameters in demarcating different dynamical regimes are presented in [Appendix B](#). We remind readers that the current study considers a wide variety of parametric combinations, some of which are being discussed for the first time. This brings out the need for developing new non-dimensional quantities that can capture effectively the effects of varying all the relevant kinematic parameters on the flow field. This is presented in the following. Generalised order-to-chaos transition boundaries are also identified in the present study in terms of the proposed non-dimensional quantities.

### 5.1. Introducing new non-dimensional quantities to capture the dynamics

As already demonstrated, the dynamical signature of the flow field is dictated primarily by the LEV separation. This, in turn, is dependent on the flapping kinematics as well as the inflow, i.e. the speed and relative orientation with which the leading edge interacts with the incoming flow. The effective AoA should be a powerful measure in this regard to define the degree of the flow separation. A novel and efficient mathematical model is proposed here to represent the entire parametric space in terms of the maximum effective AoA in one cycle ( $\alpha_{eff}^{max}$ ) and a leading-edge amplitude-based Strouhal number ( $St_{A,LE}$ ). The latter is defined as

$$St_{A,LE} = \frac{f_e A_{LE}}{U_\infty}, \quad (5.1)$$

with  $A_{LE}$  denoting the peak-to-peak amplitude of the leading edge. It can be estimated as

$$A_{LE} = 2 \times \max\{y_p(t) + x_0 \sin(\theta(t))\}. \quad (5.2)$$

These two key non-dimensional parameters,  $\alpha_{eff}^{max}$  and  $St_{A,LE}$ , are able to include both of the critical aspects discussed above – the speed and the angle with which the foil interacts with the inflow. The mathematical definitions of these two quantities include the effects of all the key kinematic and flow parameters that affect the wake dynamics. Thus changes in any of these parameters reflect directly on the  $\alpha_{eff}^{max}$ – $St_{A,LE}$  pair, which is not true for the conventionally used non-dimensional numbers defined for specific kinematic situations.

As a first step, the ( $St_{A,LE}$ ,  $\alpha_{eff}^{max}$ ) pair values corresponding to all the parametric cases presented in § 3, exhibiting periodic or chaotic dynamics, are computed and plotted

Transition boundaries and an order-to-chaos map

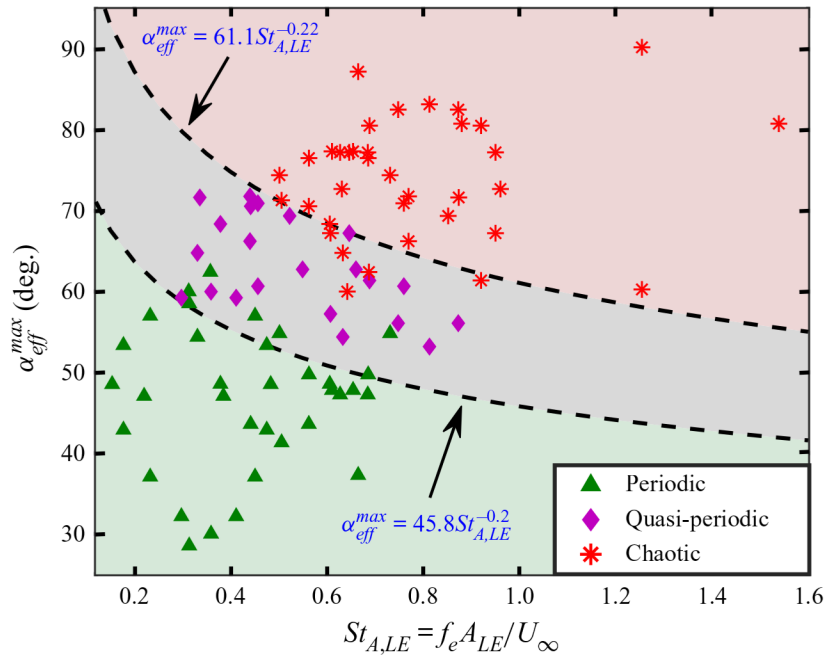


Figure 21. An order-to-chaos map ( $\alpha_{eff}^{max}$  versus  $St_{A,LE}$ ) exhibiting the three distinct regions corresponding to qualitatively different dynamical states.

in the  $\alpha_{eff}^{max}$  versus  $St_{A,LE}$  plane. It is observed that the data points belonging to the periodic and chaotic states are clustered individually in two distinct regions; see figure 21. A best fit curve  $\alpha_{eff}^{max} = 61.1 St_{A,LE}^{-0.22}$  is obtained from the boundary data of the chaotic cases using a power-law equation. This is considered as the lower boundary of the chaotic regime since all the data points belonging to the region above this curve are representative of robust chaos. Similarly, another best fit curve,  $\alpha_{eff}^{max} = 45.8 St_{A,LE}^{-0.2}$ , is obtained from the boundary data of the periodic points, and all the data points below this curve belong to the periodic regime. Thus the latter curve can be considered as the upper boundary of the periodic regime. The philosophy behind the development of these two boundaries is based on the motivation of identifying the loss of periodicity and the onset of chaos. Interestingly, all the parametric data exhibiting quasi-periodicity (transition state) in § 3 fall in the region bounded by the two above-mentioned boundary curves. Even though these boundaries are developed from the information of periodic and chaotic data points alone, the quasi-periodic points turn out to be well segregated and bounded by them. Therefore, the  $\alpha_{eff}^{max}$  versus  $St_{A,LE}$  plot in figure 21 captures efficiently the three distinct dynamical regimes, where the periodic and chaotic regimes are separated by the transitional quasi-periodic regime. It is also worth mentioning that the choice of power-law curves here is a methodological choice. Several other standard fittings were tried out as well, but the power-law fitting gave the highest accuracy. However, the exponent values in the power-law curves, i.e.  $-0.2$  for the upper bound of the periodic cases, and  $-0.22$  for the lower bound of the chaotic cases, are not by choice but are outcomes of the best-fitting process.

Dynamical transition from periodicity to robust chaos happens via local or global bifurcation routes through one or more intermediate dynamical states. The transition regime corresponds to those dynamical states for different kinematic conditions. The success of the present classification approach lies in pinpointing the periodic and robust

chaotic regions with reasonable accuracy. Fundamentally, a portion of the periodic regime may still remain ‘entangled’ with a portion of the transition regime, and similarly a portion of the chaotic regime with that of the transition regime. However, it is definitely possible to identify distinct regions of periodicity and chaos, and an in-between ‘entangled’ regime of transition dynamics. The transition regime is identified as a collection of all possible transitional states. The exact dynamics for the entire transition regime may not be known *a priori* from this classification, and one would need a case-by-case investigation to comment on that. Note that the current model to define the order-to-chaos boundaries is a first step based on the present simulations, and the main focus was to identify a reduced-order parametric space by combining the effects of the most relevant kinematic quantities and developing generalised transition boundaries in that reduced space.

In summary, a total of 100 different parametric cases were simulated in this study. Among the 36 periodic points, 30 were classified correctly, and among the 40 chaotic cases, 35 were classified correctly by the proposed transition boundaries in [figure 21](#). This gives an accuracy of more than 85 %, which is quite encouraging, especially in the light of the severe limitations of the existing non-dimensional quantities. Here are the main contributions made: (i) effective non-dimensional parameters were identified to track the qualitative changes in the flow field; (ii) a transition regime was identified where all transition states could be accommodated between order and chaos. Above this regime, robust chaos can be expected, and below, regular periodic dynamics.

### 5.2. Verification with the existing literature

In this subsection, the robustness of the proposed transition model is tested with existing data from the literature. This is demonstrated in [figure 22](#) by calculating the  $\alpha_{eff}^{max}$  and  $St_{A,LE}$  values for a series of data collected from the published results of different research groups reporting dynamical transition in flapping systems. The cases are as follows.

- (i) Lewin & Haj-Hariri (2003): pure plunging elliptic-shaped foil with 12 % thickness at  $\kappa h = 0.8, 1.0, 1.2$  and  $1.5$ , with fixed  $\kappa = 5.714$ ,  $Re = 500$ ; plotted as ■.
- (ii) Deng *et al.* (2016): pure plunging NACA0015 aerofoil at  $A_D = 2.0$  and  $Sr = 0.1$  to  $0.55$  in steps of  $0.05$ ,  $Re = 1700$ ; plotted as ►.
- (iii) Badrinath *et al.* (2017): pure plunging NACA0012 aerofoil at  $h = 0.4, 0.913$  and  $1.2$ , with fixed  $\kappa = 2.0$ ,  $Re = 1000$ ; plotted as ◀.
- (iv) Majumdar *et al.* (2020a,b): pure plunging elliptic-shaped foil with 12 % thickness at  $h = 0.25, 0.375, 0.4125$  and  $0.475$ , with fixed  $\kappa = 4.0$ ,  $Re = 300$ ; plotted as +.
- (v) Zaman *et al.* (2017): pure pitching NACA0012 aerofoil at  $\theta_0 = 20^\circ, 30^\circ, 38^\circ, 45^\circ, 50^\circ$  and  $58^\circ$ , with fixed  $\kappa = 8.0$ , with the pitching axis being at the quarter-chord location,  $Re = 500$ ; plotted as ▼.
- (vi) Lentink *et al.* (2010): simultaneous pitching–heaving elliptic foil with 5 % thickness at the dimensionless heave amplitude  $A^*(= A/c) = 1.0$  and  $2.0$  (where  $A$  is the heave amplitude),  $\alpha_0 = 15^\circ$ , dimensionless heave length  $\lambda^*(= U_\infty/fc) = 3$  to  $13$  in steps of  $2$ ,  $\phi = \pi/2$ , with the pitching axis being at the mid-chord location,  $Re = 1000$ ; plotted as ×.
- (vii) Bose & Sarkar (2018): simultaneous pitching–plunging NACA0012 aerofoil at  $h = 0.5, 0.85$  and  $1.25$ ,  $\alpha = 15^\circ$ ,  $\kappa = 2.0$ ,  $\phi = \pi/2$ , with the pitching axis being at the quarter-chord location,  $Re = 1000$ ; plotted as ●.

## Transition boundaries and an order-to-chaos map

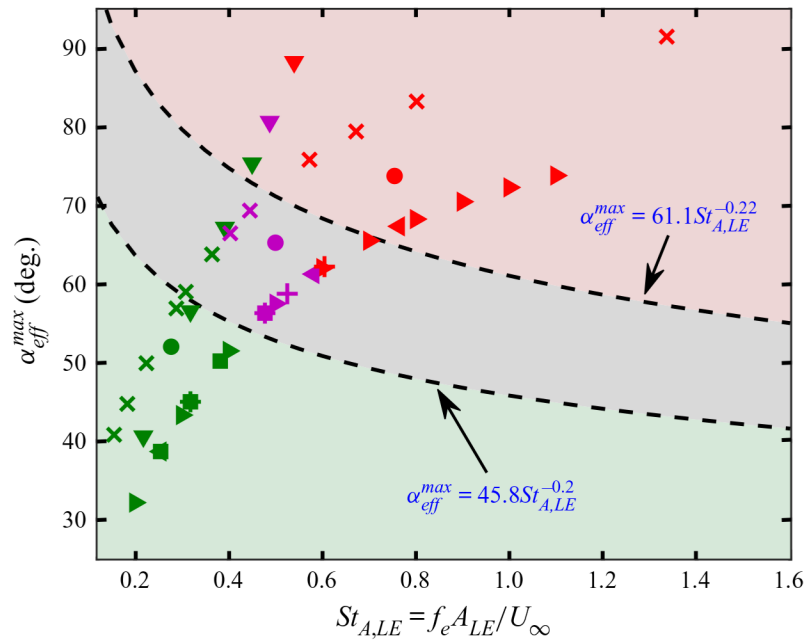


Figure 22. Validating the proposed transitional boundaries with the reporting of earlier works by different research groups. Markers are used as follows:  $\blacksquare$ , Lewin & Haj-Hariri (2003);  $\blacktriangleright$ , Deng *et al.* (2016) (pure plunge);  $\blacktriangleleft$ , Badrinath *et al.* (2017);  $+$ , Majumdar *et al.* (2020a,b);  $\blacktriangledown$ , Zaman *et al.* (2017);  $\times$ , Lentink *et al.* (2010); and  $\bullet$ , Bose & Sarkar (2018). Colourcode: green if the dynamical state corresponding to the data point was reported to be periodic, red if it was reported to be chaos, and purple if the reported dynamical state exhibited transitional signature in the respective literature.

The mathematical symbols used in the above description are as given in their respective articles. The markers in figure 22 are colour coded based on the dynamical states reported in the respective literature, i.e. green if the data point was reported as periodic, red if it was reported as chaotic, and purple if the data point was transitional. As described in the previous paragraph, the cases taken from the literature involve various combinations of different kinematic parameters, flapping motions (pure plunge, pure pitch, simultaneous pitch–plunge), foil shapes and thicknesses, etc. Despite the variety of the parametric combinations, their dynamical states corroborate very well the proposed transitional boundaries, giving credibility to the present order-to-chaos map. A few exceptions have also been observed in the case of pure pitching at  $\theta_0 = 45^\circ$  and  $50^\circ$  from Zaman *et al.* (2017). Among the 42 cases taken from the literature, 15 data points have been identified as periodic as per the present model, and all of them were also reported to be periodic in their respective studies. On the other hand, out of the 13 data points that fall above the shaded transition region as chaotic, only 11 were actually called chaotic in their respective studies. Thus out of 28 cases, 26 have been classified correctly, demonstrating an accuracy of around 93%. These results strengthen the efficacy of the proposed transition boundaries for demarcating the periodic and chaotic parametric sets in terms of  $\alpha_{eff}^{max}$  and  $St_{A,LE}$ .

## 6. Conclusions

Effects of a wide variety of kinematic conditions on the dynamical transition in the wake of a flapping foil have been investigated by simulating a large number of parametric combinations (a total of 100 different cases) using an IBM-based in-house Navier–Stokes solver. It has been established already in the literature that the plunge amplitude and

flapping frequency are two essential parameters that can dictate the dynamical nature of the flow field. This study reveals that other parameters, such as pitch amplitude ( $\theta_0$ ), pitching axis location ( $x_0$ ), foil thickness, type of kinematics, and phase offset ( $\phi$ ) between pitch and plunge motions, can also play very important roles in influencing the wake dynamics. The present study has also established that the chaotic transition in the flow field is strongly correlated with the strength of the primary LEV. Beyond a certain strength, the growth and separation of the LEV structure become chaotic, which eventually gets propagated to the trailing wake through LEV–TEV interactions in the subsequent cycles.

One of the main contributions of the present study is the introduction of two new non-dimensional quantities ( $St_{A,LE}$  and  $\alpha_{eff}^{max}$ ) to capture the physical effect of the parametric variations considered in the study. The proposed dimensionless parameters can capture the important effects of the speed and the angle with which the foil interacts with the inflow. Changes in key parametric quantities reflect directly on the  $\alpha_{eff}^{max}$ – $St_{A,LE}$  pair, which is not true for the conventionally used non-dimensional numbers defined in the literature for specific kinematic situations. The other important contribution of the study is to propose generalised transition boundaries and an order-to-chaos map in terms of the newly proposed non-dimensional parameters. Published data from the existing literature have also been utilised to confirm the proposed boundaries. Despite the wide variety of parametric combinations, the dynamical states from both new and published data corroborate very well the proposed transitional boundaries, giving credibility to the order-to-chaos map.

**Supplementary material.** Supplementary materials are available at <https://doi.org/10.1017/jfm.2022.385>.

**Declaration of interest.** The authors report no conflict of interest.

**Author ORCIDs.**

-  Dipanjan Majumdar <https://orcid.org/0000-0002-3551-3768>;
-  Chandan Bose <https://orcid.org/0000-0001-5166-9968>;
-  Sunetra Sarkar <https://orcid.org/0000-0003-0331-0138>.

**Appendix A**

The derivation of  $\alpha_{eff}$  is given here. For any point on the chord line located at a distance  $s$  from the leading edge, its position along the  $y$ -direction can be written as

$$y_s = y_p - (s - x_0) \sin \theta. \tag{A1}$$

Note that the pitch motion is clockwise positive, and plunge is positive along the positive  $y$ -axis. The velocity at the  $s$  location can be obtained from the time derivation of (A1) as

$$\dot{y}_s = \dot{y}_p - (s - x_0)\dot{\theta} \cos \theta. \tag{A2}$$

Hence the average downwash velocity induced by the entire chord can be estimated as

$$W = -\frac{\int_0^c \dot{y}_s ds}{\int_0^c ds} = -\frac{1}{c} \int_0^c \{\dot{y}_p - (s - x_0)\dot{\theta} \cos \theta\} ds = -\left[\dot{y}_p - \left(\frac{c}{2} - x_0\right)\dot{\theta} \cos \theta\right]. \tag{A3}$$

Finally, the effective AoA is given by

$$\alpha_{eff} = \theta - \tan^{-1} \left[ \frac{W}{U_\infty} \right] = \theta - \tan^{-1} \left[ \frac{1}{U_\infty} \left\{ \dot{y}_p - \left(\frac{c}{2} - x_0\right)\dot{\theta} \cos \theta \right\} \right]. \tag{A4}$$

## Transition boundaries and an order-to-chaos map

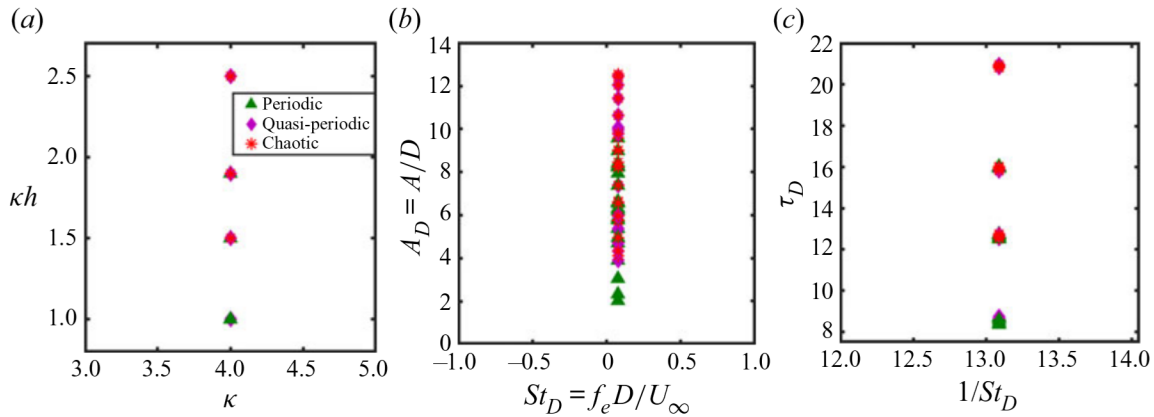


Figure 23. The parametric cases of § 3.3.1 presented in terms of the conventional non-dimensional numbers used by different research groups.

## Appendix B

Figure 23(a) presents a plot in terms of non-dimensional parameters  $\kappa h$  versus  $\kappa$  for all the parametric cases discussed in § 3.3.1. All those parametric cases collapse on just four data points ( $\kappa h = 1.0, 1.5, 1.9, 2.5$ ). Evidently, the different dynamical states that belong to these parametric combinations ( $\phi$  variation) cannot be distinguished through these non-dimensional parameters. Similarly, non-dimensional parameters  $A_D$  and  $St_D$  (proposed by Godoy-Diana *et al.* 2009) are also not suitable. The  $A_D$  versus  $St_D$  plot for the same cases is shown in figure 23(b). Here, the data points get mixed up and no pattern can be identified for the different dynamical states involved. As in these parametric cases  $f_e$ ,  $D$  and  $U_\infty$  were not changed, a constant  $St_D = 0.0764$  appears for all the cases, and the  $A_D$  value hovers within the range  $2.01 < A_D < 12.57$ . Note that for a given  $\kappa h$ , a  $\phi$  pair that is symmetric about the zero mean line (such as  $\phi = \pi/4$  &  $7\pi/4$  or  $\phi = \pi/2$  &  $3\pi/2$ ) result in the same  $A_D$ , even though the pair may exhibit very different dynamics. As was shown in figure 8,  $\phi = \pi/2$  and  $\phi = 3\pi/2$  at  $\kappa h = 0.375$  manifest different dynamics (periodic and chaotic, respectively), though both have the same  $A_D$  value of 6.62. A  $\tau_D$  versus  $1/St_D$  plot has also been made here in figure 23(c), as proposed by Lagopoulos *et al.* (2019). No clear demarcation between the different dynamical states can be found here either. Thus in the light of the above discussion, the limitations of the earlier approaches in demarcating different dynamical regimes encountered presently are evident.

## Appendix C

The effect of pivot location on the dynamical states of the flow field is small at  $\phi = \pi/2$  and  $3\pi/2$ , but it is quite tangible for  $\phi = \pi$  and  $2\pi$ . In order to understand the different trends at different  $\phi$ , one needs to look into the respective  $(St_{A,LE}, \alpha_{eff}^{max})$  pair values. This is because these quantities capture the two critical aspects – the leading-edge speed and the relative orientation with which the foil interacts with the incoming flow – that are the fundamental factors that affect the LEV formation and growth, and in turn, dictate the dynamical characteristics of the flow field. Figure 24 shows the  $(St_{A,LE}, \alpha_{eff}^{max})$  pairs corresponding to the 12 parametric cases obtained by varying  $\phi$  and  $x_0$  (as presented in § 3.3.3). The cases corresponding to  $x_0 = 0.25, 0.5$  and  $0.75$  are plotted using the markers  $+$ ,  $\blacksquare$  and  $\bullet$ , respectively. The markers are colour coded as green, purple or red if they appear to be periodic, quasi-periodic or chaotic from the flow simulations, respectively.

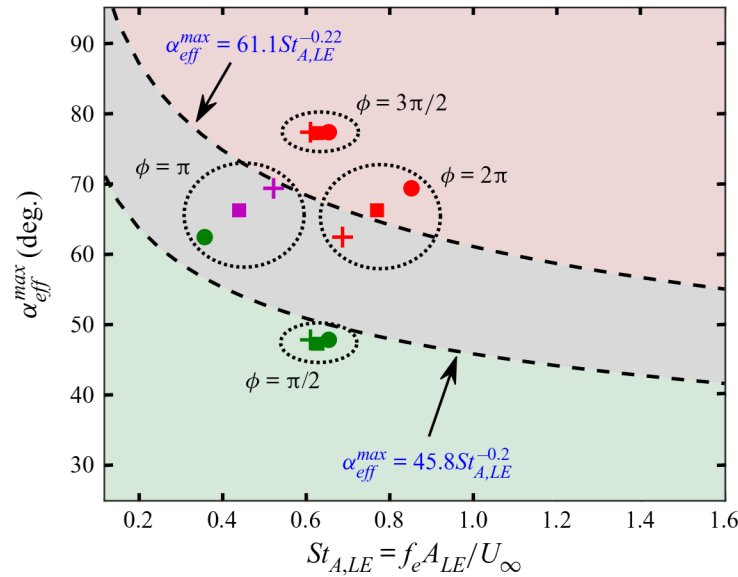


Figure 24. Variation in  $(St_{A,LE}, \alpha_{eff}^{max})$  pairs as the pivot location and phase offset are varied. Cases corresponding to  $x_0 = 0.25, 0.5$  and  $0.75$  are plotted using the markers  $+$ ,  $\blacksquare$  and  $\bullet$ , respectively. The markers are colour coded as green, purple or red if they appear to be periodic, quasi-periodic or chaotic from the flow simulations, respectively.

Note that in figure 24, the three data points at  $\phi = \pi/2$  are seen to be sufficiently inside the periodic regime and are close to each other. This implies that these three cases correspond to sufficiently low leading-edge speed and effective AoA, and are thus associated with a stable periodic LEV behaviour. This results in periodic flow fields. At  $\phi = 3\pi/2$ , the three data points corresponding to three different  $x_0$  values are sufficiently inside the chaotic regime and are close to each other (figure 24). These cases correspond to substantially high leading-edge speed and effective AoA, and as a result are associated with chaotic LEV growth resulting ultimately in chaotic flow fields. Hence the dynamics at  $\phi = \pi/2$  and  $\phi = 3\pi/2$  look largely independent of the pivot location.

The cases of  $\phi = \pi$  and  $\phi = 2\pi$  fall in the transition regime. At  $\phi = \pi$ , as the pivot point is moved from the quarter-chord to the three-quarter-chord location, both  $St_{A,LE}$  and  $\alpha_{eff}^{max}$  gradually decrease, and the data points move towards the periodic regime; see figure 24. This is because the flapping motion at this  $\phi$  is such that the leading edge traverses comparatively smaller distance with a lower leading-edge speed, and takes lower effective AoA values as the pivot point moves towards the trailing edge. As a result, gradually more stable primary LEV structures are formed with increasing  $x_0$ , and therefore the flow field turns from quasi-periodic to periodic. At  $\phi = 2\pi$ ,  $St_{A,LE}$  and  $\alpha_{eff}^{max}$  increase, and the data points move towards the chaotic regime with an increase in  $x_0$  (figure 24). At this  $\phi$ , the leading edge traverses higher distances with increased leading-edge speed, and the foil takes comparatively higher effective AoA values as  $x_0$  increases. This leads to irregular formation of the primary leading-edge vortices having higher strength and more agility, which eventually make the overall flow field more irregular, as observed in § 3.3.3. In conclusion, movement of the pivot location from the leading edge towards the trailing edge affects the leading-edge flapping speed and the foil's relative orientation with respect to the incoming flow conversely for  $\phi = \pi$  and  $2\pi$ . Hence the flow field behaves contrastingly at these two  $\phi$  values. It gets regularised at  $\phi = \pi$ , but becomes more and

more irregular at  $\phi = 2\pi$  with increasing  $x_0$ . This explains the underlying reason behind the opposite trends of the dynamical states at  $\phi = \pi$  and  $2\pi$  observed in § 3.3.3.

REFERENCES

- ANDERSON, J.M., STREITLIEN, K., BARRETT, D.S. & TRIANTAFYLLOU, M.S. 1998 Oscillating foils of high propulsive efficiency. *J. Fluid Mech.* **360**, 41–72.
- ASHRAF, M.A., YOUNG, J. & LAI, J.C.S. 2012 Oscillation frequency and amplitude effects on plunging airfoil propulsion and flow periodicity. *AIAA J.* **50** (11), 2308–2324.
- BADRINATH, S., BOSE, C. & SARKAR, S. 2017 Identifying the route to chaos in the flow past a flapping airfoil. *Eur. J. Mech. (B/Fluids)* **66**, 38–59.
- BOSE, C., GUPTA, S. & SARKAR, S. 2021 Dynamic interlinking between near- and far-field wakes behind a pitching–heaving airfoil. *J. Fluid Mech.* **911**, A31.
- BOSE, C. & SARKAR, S. 2018 Investigating chaotic wake dynamics past a flapping airfoil and the role of vortex interactions behind the chaotic transition. *Phys. Fluids* **30** (4), 047101.
- BUREN, T.V., FLORYAN, D. & SMITS, A.J. 2019 Scaling and performance of simultaneously heaving and pitching foils. *AIAA J.* **57** (9), 3666–3677.
- CALDERON, D.E., CLEAVER, D.J., GURSUL, I. & WANG, Z. 2014 On the absence of asymmetric wakes for periodically plunging finite wings. *Phys. Fluids* **26** (7), 349–376.
- CLEAVER, D.J., WANG, Z. & GURSUL, I. 2012 Bifurcating flows of plunging aerofoils at high Strouhal numbers. *J. Fluid Mech.* **708**, 349.
- DENG, J., SUN, L., TENG, L., PAN, D. & SHAO, X. 2016 The correlation between wake transition and propulsive efficiency of a flapping foil: a numerical study. *Phys. Fluids* **28** (9), 094101.
- GODOY-DIANA, R., MARAIS, C., AIDER, J.-L. & WESFREID, J.E. 2009 A model for the symmetry breaking of the reverse Bénard–von Kármán vortex street produced by a flapping foil. *J. Fluid Mech.* **622**, 23–32.
- GROSSMANN, A., KRONLAND-MARTINET, R. & MORLET, J. 1990 Reading and understanding continuous wavelet transforms. In *Wavelets*, pp. 2–20. Springer.
- GUSTAFSON, K. & LEBEN, R.R. 1988 Robust multigrid computation and visualization of separation and vortex evolution in aerodynamic flows. In *1st National Fluid Dynamics Conference, (AIAA/ASME/SIAM/APS)*, No. AIAA-88-3604-CP, AIAA, Washington, D.C., pp. 174–184.
- HILBORN, R.C., *et al.* 2000 *Chaos and Nonlinear Dynamics: An Introduction for Scientists and Engineers*. Oxford University Press on Demand.
- JONES, K.D., DOHRING, C.M. & PLATZER, M.F. 1998 Experimental and computational investigation of the Knoller–Betz effect. *AIAA J.* **36** (7), 1240–1246.
- KENNEL, M.B., BROWN, R. & ABARBANEL, H.D.I. 1992 Determining embedding dimension for phase-space reconstruction using a geometrical construction. *Phys. Rev. A* **45** (6), 3403.
- KIM, J., KIM, D. & CHOI, H. 2001 An immersed-boundary finite-volume method for simulations of flow in complex geometries. *J. Comput. Phys.* **171** (1), 132–150.
- LAGOPOULOS, N.S., WEYMOUTH, G.D. & GANAPATHISUBRAMANI, B. 2019 Universal scaling law in drag-to-thrust wake transition of flapping foils. *J. Fluid Mech.* **872**, R1.
- LEE, T. & SU, Y.Y. 2015 Surface pressures developed on an airfoil undergoing heaving and pitching motion. *J. Fluids Engng* **137** (5), 051105.
- LENTINK, D., VAN HEIJST, G.F., MUIJRES, F.T. & VAN LEEUWEN, J.L. 2010 Vortex interactions with flapping wings and fins can be unpredictable. *Biol. Lett.* **6** (3), 394–397.
- LEWIN, G.C. & HAJ-HARIRI, H. 2003 Modelling thrust generation of a two-dimensional heaving airfoil in a viscous flow. *J. Fluid Mech.* **492**, 339–362.
- MAJUMDAR, D., BOSE, C. & SARKAR, S. 2020a Capturing the dynamical transitions in the flow-field of a flapping foil using immersed boundary method. *J. Fluids Struct.* **95**, 102999.
- MAJUMDAR, D., BOSE, C. & SARKAR, S. 2020b Effect of gusty inflow on the jet-switching characteristics of a plunging foil. *Phys. Fluids* **32** (11), 117105.
- MARWAN, N., ROMANO, M.C., THIEL, M. & KURTHS, J. 2007 Recurrence plots for the analysis of complex systems. *Phys. Rep.* **438** (5-6), 237–329.
- READ, D.A., HOVER, F.S. & TRIANTAFYLLOU, M.S. 2003 Forces on oscillating foils for propulsion and maneuvering. *J. Fluids Struct.* **17** (1), 163–183.
- STREITLIEN, K. & TRIANTAFYLLOU, G.S. 1998 On thrust estimates for flapping foils. *J. Fluids Struct.* **12** (1), 47–55.
- TRIANAFYLLOU, M.S., TRIANTAFYLLOU, G.S. & GOPALKRISHNAN, R. 1991 Wake mechanics for thrust generation in oscillating foils. *Phys. Fluids* **3** (12), 2835–2837.



- VISBAL, M.R. 2009 High-fidelity simulation of transitional flows past a plunging airfoil. *AIAA J.* **47** (11), 2685–2697.
- WILLIAMSON, C.H.K. & ROSHKO, A. 1988 Vortex formation in the wake of an oscillating cylinder. *J. Fluids Struct.* **2** (4), 355–381.
- ZAMAN, R., YOUNG, J. & LAI, J.C.S. 2017 Oscillating foils with high pitch amplitudes. In *The 28th International Symposium on Transport Phenomena*.
- ZHENG, Z.C. & WEI, Z. 2012 Study of mechanisms and factors that influence the formation of vortical wake of a heaving airfoil. *Phys. Fluids* **24** (10), 103601.
- ZURMAN-NASUTION, A.N., GANAPATHISUBRAMANI, B. & WEYMOUTH, G.D. 2020 Influence of three-dimensionality on propulsive flapping. *J. Fluid Mech.* **886**, A25.